Institut für Kernphysik

Mathematisch-Naturwissenschaftliche Fakultät
Universität zu Köln

Detection of high-energy muons from cosmic rays with a highly-segmented HPGe detector

Master Thesis
August 4, 2014

David Schneiders

Advisor: Prof. Dr. P. Reiter

Abstract

Knowledge about the properties of secondary particles originating from radioactive ion beams is of very high importance for γ-ray spectroscopy with the Advanced GAmma Tracking Array (AGATA).
The newly constructed dual gain preamplifier for the AGATA setup enables a vast improvement of the dead time caused by secondary particles. In this work, the main properties of this preamplifier were tested in a fully operational experimental system.
By using the widely expanded energy range of up to 180 MeV of the new preamplifier, energy depositions of naturally abundant cosmic rays inside a HPGe detector could be analysed for the first time. The experiment verified the muonic character of the radiation by calculating the specific energy loss of the incident particles.
The 36-fold segmentation of the AGATA detectors was used to track the trajectories of the muons. By analysing the individual segment voltage signals, a finer tracking was achieved. Thus, it was possible to divide all 36 segments into 4 subsegments, 144 trackable subsegments in total. Inside the 72 inner subsegments a space resolved tracking along the radial component is possible.

Zusammenfassung

Die Kenntnis der Eigenschaften von Sekundärteilchen aus radioaktiven Ionenstrahlen ist sehr wichtig für γ-Spektroskopie mit dem Advanced GAmma Tracking Array (AGATA).
Der für das AGATA-Setup neuartig entwickelte Dual-Gain-Vorverstärker ermöglicht eine immense Verbesserung der von Sekundärteilchen verursachten Totzeit im Messsystem. In dieser Arbeit wurden die Haupteigenschaften des Vorverstärkers in einem voll funktionsfähigen System getestet.
Durch Ausnutzen des bis 180 MeV stark erweiterten Energiemessbereiches konnten die Energiedepositionen von natürlich verfügbaren kosmischen Strahlen innerhalb eines HPGe-Detektors zum ersten Mal analysiert werden. Das Experiment konnte den myonischen Charakter der Höhenstrahlung durch Berechnung des spezifischen Energieverlusts der eintreffenden Teilchen im Germanium bestätigen.
Um die Trajektorien der Myonen nachzuvollziehen (*Tracking*), wurde die 36-fache Segmentierung der AGATA-Detektoren ausgenutzt. Indem die individuellen Spannungssignale in den Segmenten untersucht wurden, konnte ein genaueres Tracking erzielt werden. Es war daher möglich, die 36 Segment in jeweils 4 Untersegmente aufzuteilen, so dass insgesamt 144 Untersegmente zur Verfügung standen. Innerhalb der 72 inneren Untersegmente ist ein ortsaufgelöstes Tracking entlang der radialen Komponente möglich.

Contents

1 Motivation

The properties of muons are well studied [11, 14]. Cosmically generated muons will be used to calibrate an experimental setup which will be operated in facilities with radioactive ion beams. The AGATA setup [8] is a HPGe array for high-performance γ-ray spectroscopy. Naturally abundant cosmic rays can be used as a calibration source for these higher energy regimes which cannot be covered by conventional calibration sources. For this purpose, a new dual gain preamplifier has been constructed.

Due to the secondary particle production of radioactive ion beams, the preamplifier is provided with a fast reset circuit. This circuit enables the preamplifier to desaturate the experimental system in the case of large energy depositions caused by heavier particles. Thus, the dead time of the system can be vastly reduced and the array is able to perform γ-ray spectroscopy with a very high energy resolution.

This work will investigate the effects of cosmic rays on a fully operational AGATA HPGe detector. The study focuses on the characterization of the incident radiation and tracking of the particles' trajectories via the segmentation of the detector and a newly constructed dual gain preamplifier.

2 Cosmic Rays

2.1 Production and Composition

In general cosmic rays are divided into two groups: primary cosmic and secondary terrestric rays.

Primary cosmic rays These cosmic rays typically consist of charged particles and nuclei which are produced in stellar fusion and are accelerated by strong electromagnetic fields as well as novae of stars. Therefore primary cosmic radiation contains electrons, protons, helium, carbon, oxygen and heavier elements up to iron. Predominantly it is composed of: protons (up to 90%), alpha particles (9%), electrons ($<1\%$) and heavier nuclei (up to 0.25%). Cosmic rays are strongly dominated by matter and therefore show a clear sign for the asymmetry of matter and antimatter in the universe. Moreover it is assumed that most of the antimatter in the primary cosmic radiation (e.g. positrons) originates from high energy particle reactions outside the atmosphere [17].
Most cosmic rays hitting the earth's atmosphere have an energy of $E < 1\,\mathrm{GeV}$ and originate from our sun and its solar winds, whereas particles with $E > 1\,\mathrm{GeV}$ stem from extrasolar or even extragalactic sources. All extrasolar particles are affected by the sun and its winds. Therefore particles with low energies (up to several GeV) can only be detected in phases of low solar activity. For those particles it is not possible to overcome the forces caused by the sun and the earth's magnetic field. High-energy particles (up to $10^{20}\,\mathrm{eV}$) also are affected by these forces, but due to their energy far less significantly. Thus, the particle flux depends on date, time and geographical location of the measurements.

Secondary cosmic rays Basically all primary particles interact with particles in the upper layers of the atmosphere (strato-mesosphere and lower thermosphere, altitude range of $30 - 50\,\mathrm{km}$) by entering the earth's atmosphere. These interactions are mainly spallation reactions of heavier nuclei (e.g. $^{14}\mathrm{N}$, $^{16}\mathrm{O}$, ...) starting cascades of lighter particles.

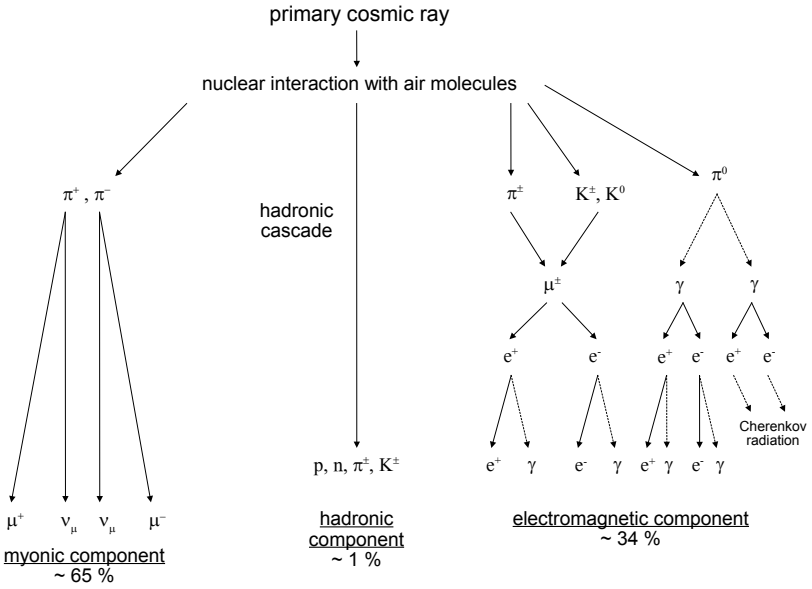

Figure 2.1: Interacting with molecules in the upper atmosphere primary cosmic rays produce cascades of lighter particles. Electromagnetic and hadronic components amount to 35% of total particle fluxes. Neutrinos produced in the branch of electromagnetic cascades are not shown for reasons of presentability (adapted from [17], ratios from [14]).

In high-energy proton collisions kaons and, due to strangeness conservation, Λ-baryons are produced. The neutral Λ-baryons typically decay into a nucleon and a pion (branching ratio BR taken from [11]).

$$\begin{aligned} \Lambda &\to \mathrm{p} + \pi^- \quad \text{BR } (63.9 \pm 0.5\%) \\ \Lambda &\to \mathrm{n} + \pi^0 \quad \text{BR } (35.8 \pm 0.5\%) \end{aligned}$$

Positive and negative kaons have also two main decay modes (BR $> 5\%$, [11]). In the first mode kaons decay into a muon equal in charge and a muon neutrino due to conservation of lepton number. In the second mode kaons decay into two pions, one neutral and one corresponding to the kaons charge. Neutral kaons decay into a combination of multiple pions.

$$\mathrm{p} + \mathrm{p} \to \mathrm{p} + \Lambda + K^+$$

$$\begin{aligned} \mathrm{K}^+ &\to \mu^+ + \nu_\mu \quad \text{BR } (63.55 \pm 0.11\%) \\ \mathrm{K}^+ &\to \pi^+ + \pi^0 \quad \text{BR } (20.66 \pm 0.08\%) \end{aligned}$$

$$\begin{aligned} \mathrm{K}^- &\to \mu^- + \overline{\nu}_\mu \quad \text{BR } (63.55 \pm 0.11\%) \\ \mathrm{K}^- &\to \pi^- + \pi^0 \quad \text{BR } (20.66 \pm 0.08\%) \end{aligned}$$

The resulting pions themselves decay with a high probability into a muon with the same (positive or negative) charge and a muon neutrino via weak interaction. Due to phase space arguments and energy efficiency, the decay into a positron (or electron) and an electron (anti)neutrino would be favoured. However, the electronic decay is strongly suppressed by helicity violation. Neutral pions are a linear combination of the quark pairs $u\bar{u}$ and $d\bar{d}$. Therefore they decay much faster via the electromagnetic interaction into two photons or (rarely) into an electron-positron-pair and a photon.

$$\pi^+ \to \mu^+ + \nu_\mu$$
$$\pi^- \to \mu^- + \overline{\nu}_\mu$$

$$\pi^0 \to 2\,\gamma$$
$$\pi^0 \to \mathrm{e}^+ + \mathrm{e}^- + \gamma$$

These various decay mechanisms can explain the very different lifetimes of pions. Neutral pions exist for about $10^{-17}\,\mathrm{s}$, whereas charged pions exist for about $10^{-8}\,\mathrm{s}$. Additionally, the critical kinetic energy of pions amounts to $\epsilon_\pi = 115\,\mathrm{GeV}$. Below this threshold, a pion's velocity is so small that its decay length is shorter then its interaction length. Thus, it rather decays instead of interacting with other atmospheric particles. Above the critical energy pions can produce cascades of secondary rays by interaction with atmospheric matter before decaying.
Muons produced in kaon and pion decay can decay on their way to earth's surface. A negative charged muon decays with a rate of 100% into an electron, an electron antineutrino and a muon neutrino. The decay for a positive muon is the charge conjugate of the negative muon's decay.

$$\mu^- \to \mathrm{e}^- + \overline{\nu}_\mathrm{e} + \nu_\mu$$
$$\mu^+ \to \mathrm{e}^+ + \nu_\mathrm{e} + \overline{\nu}_\mu$$

Muons, electrons and photons originating from all these decays form the main part of the secondary cosmic rays which can be detected on earth's surface and in the lower layers of the atmosphere. High-energy primary cosmic rays, particles of the hadronic component of the secondary cosmic rays, pions and neutrinos may penetrate the atmosphere. However, they form only a very small part of cosmic rays or simply are rarely detectable [11, 20].

2.2 Interaction of Cosmic Rays with Earth's Surface

2.2.1 Muonic Component

As mentioned in the last paragraph, only two substituents of cosmic rays are able to reach earth's surface in a significant amount: muons and neutrinos. Neutrinos are hard to detect due to their extremely small interaction probability with matter ($\sigma \approx 10^{-14}\,\mathrm{b/GeV}$, [12]). Muons can penetrate earth's atmosphere completely due to their high kinetic energy and the principles of the special theory of relativity. The average lifetime of a muon is $\tau = 2.2 \cdot 10^{-6}\,\mathrm{s}$. Produced at an altitude of $30 - 50\,\mathrm{km}$, a muon could (practically) never reach earth's surface before decaying using the principles of classical physics. But they move with very high velocities ($v > 0.99c$) and relativistic effects like time dilatation come into play. The mentioned lifetime of a muon is measured in its rest frame. Indeed, the muons' velocity is so high that the time dilatation extends its lifetime to $\tau = 1.6 \cdot 10^{-5}\,\mathrm{s}$, measured in the laboratory frame. So they can reach earth's surface easily and are even able to penetrate solid rock, etc. up to several hundred meters. The interaction of muons with matter (their *stopping power*) can be described as for all heavy charged particles by the following formula from [14]:

$$\left\langle -\frac{dE}{dx} \right\rangle = a(E) + b(E)E = 2a(E)|_{E=E_{\mu c}} \tag{2.1}$$

The functions $a(E)$ and $b(E)$ are slowly varying and depend on the muon energy. $a(E)$ describes electronic losses and $b(E)$ radiative processes. Radiative processes take into account bremsstrahlung, e^+-e^--pair production and photonuclear interactions. The critical energy $E_{\mu c}$ for muons can be obtained by a and b:

$$a(E_{\mu c}) = E_{\mu c}\, b(E_{\mu c}) \tag{2.2}$$

The critical energy of a charged particle gives a threshold at which ionizing and radiative losses give equal contribution to the stopping power.
Figure 2.2 shows the stopping power of muons in germanium. Radiative losses start at the minimum at around 257 MeV. This minimum is also called *minimum ionization*. Up to this energy muon stopping only takes place via ionization. Muons with this kinetic energy experience a stopping power of $-\,dE/dx = 1.371\,\mathrm{MeV\,cm^2\,g^{-1}}$ in germanium [14]. At sea level muons are usually observed with a kinetic energy around this value. Radiative losses start to take place at minimum ionization and begin to dominate at the critical energy $E_{\mu c} = 295\mathrm{GeV}$, as indicated in figure 2.2.

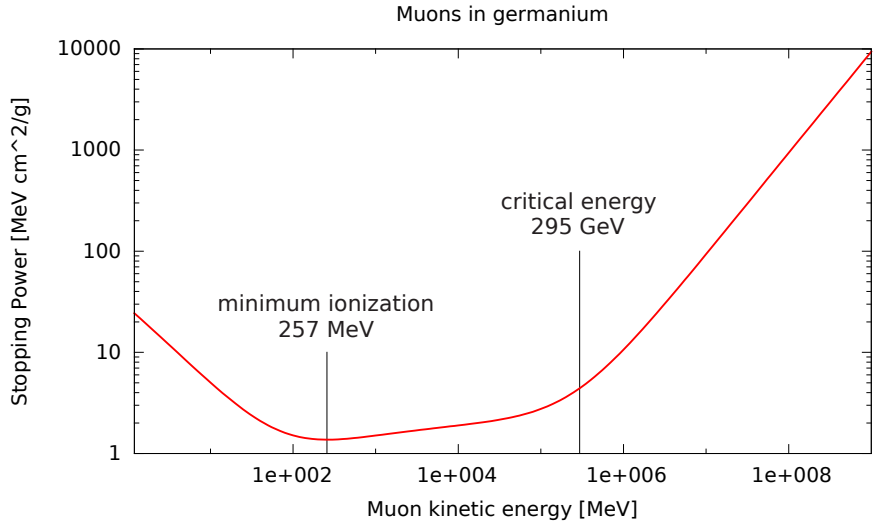

Figure 2.2: Stopping power of muons in germanium as a function of the muon energy. The main part up to the critical energy is well described by the Bethe formula. For higher energies radiative processes like bremsstrahlung dominate. Muons observed at sea level usually have kinetic energies in the range of the minimum ionization. Data were taken from [14].

Below 1 MeV kinetic energy the stopping power of muons can be described by the theory of Lindhard-Scharff [16] and Andersen-Ziegler [3]. From this energy up to $E_{\mu c}$ the energy dependence follows the classic Bethe formula without correction terms [4]:

$$-\frac{dE}{dx} = \frac{4\pi}{m_e c^2} \cdot \frac{nz^2}{\beta^2} \cdot \left(\frac{e^2}{4\pi\epsilon_0}\right)^2 \cdot \left[\ln\left(\frac{2m_e c^2\beta^2}{I \cdot (1-\beta^2)}\right) - \beta^2\right] \tag{2.3}$$

In section 4.2 a simplified version of this formula will be used to calculate the energy depositions of muons in a detector system.

According to [10], the integral intensity of muons travelling in vertical direction with momenta above 1 GeV/c amounts to $I \approx 70\,\mathrm{m^{-2}s^{-1}sr^{-1}}$. As a rule of thumb, one can assume an intensity of $I \approx 1\,\mathrm{cm^{-2}min^{-1}}$ to be measured in experiments. In this estimation the solid angle is no longer taken into account as it only depends on the distance between the measuring area and earth's centre. Typically this distance is orders of magnitude larger than the differences in altitude for different experiments. Thus, the solid angle can be assumed to be constant. Other factors are more important. Earth's magnetic field and (in connection to this) the geographical latitude of the experiment influence the muon flux. Due to a so called bottle neck at earth's magnetic poles the muon flux decreases with lower latitudinal values [7, 20].

2.2.2 Hadronic Component

Nucleons hitting earth's surface are generally residues of primary cosmic rays or scattered initiators of secondary radiation. In contrast to muons and neutrinos, hadronic particles do not penetrate solid materials deeply. They react in a much faster way with matter, mainly by collisions and are therefore stopped effectively. Hence, a measuring system inside a closed laboratory should not be affected by the hadronic component. However, the intensity outside a laboratory is much smaller than for the muonic component and amounts to $I \approx 0.9\,\mathrm{m^{-2}s^{-1}sr^{-1}}$ [10].

2.2.3 Electromagnetic Component

The electromagnetic component consists of electrons, positrons and photons, which are produced in decay reactions of secondary cosmic rays, e.g. muons and pions. Electrons and positrons are shielded by matter almost as efficient as the hadronic particles. Photons show different interactions with matter, depending on their energy. The most probable interactions in the energy regime above 1 MeV are Compton scattering and pair production. Moreover, high-energy γ-rays with $E_\gamma > 5\,\mathrm{MeV}$ also lead to photonuclear disintegration. However, in a lab surrounded by reinforced concrete, most of the photons should be shielded. Nevertheless, due to the Lambert-Beer law, some high-energy γ-rays can affect the measuring system. The vertical intensity of the electromagnetic component outside a laboratory decreases strongly with increasing energy [10]:

$$\begin{aligned} I &\approx 30\ \mathrm{m^{-2}s^{-1}sr^{-1}} \quad \text{from} \quad 10\ \mathrm{MeV} \\ I &\approx 6\ \mathrm{m^{-2}s^{-1}sr^{-1}} \quad \text{from} \quad 100\ \mathrm{MeV} \\ I &\approx 0.2\ \mathrm{m^{-2}s^{-1}sr^{-1}} \quad \text{from} \quad 1000\ \mathrm{MeV} \end{aligned}$$

3 Experimental Setup

3.1 HPGe Detector

For the experiments performed for this thesis, the 36-fold segmented High Purity Germanium (*HPGe*) detector A008 from the AGATA collaboration was used. The exact principle of operation of such a complex detector is documented in detail in the literature [8, 21] and will not be reproduced in full length here. Nevertheless, some of the important points for following analysis steps will be pointed out.
The first feature of the detector system itself is a newly developed *dual gain preamplifier* for the central core electrode of the HPGe. This preamplifier and a new analysis method for energy depositions in the MeV range, the *Time over Threshold* method (short *ToT*), will be discussed in detail below.
The second important feature is the high segmentation of the HPGe detector. It is electrically divided into six times six segments, in total 36. The segmentation is illustrated in figure 3.2 in the upper left. Six individual *rings* are depicted in different colors (left to right: 1 to 6 in AGATA notation [21]), in contrast to the six *sectors* which in this picture reach from black to pink (A to F in AGATA notation). These italic annotations are reused in chapters below. With this segmentation it is possible to track trajectories of incoming (not stopped) particles interacting with the detector material. This rough tracking only by hit segments can be improved by weighting so called transients in neighbouring segments of the particle track.

3.2 Dual Gain Preamplifier

The dual gain preamplifiers are specially and exclusively designed for the 36-fold segmented HPGe detectors used by the AGATA collaboration. They are built for two purposes: expanding the energy range of the core electrode and reducing the dead time of the system caused by high energy secondary particles from radioactive beam experiments at relativistic energies. The widely expanded energy range allows highly efficient and high resolution γ-ray spectroscopy in order to find exotic and highly excited energy and spin transitions. Figure 3.1 shows a picture of the preamplifier

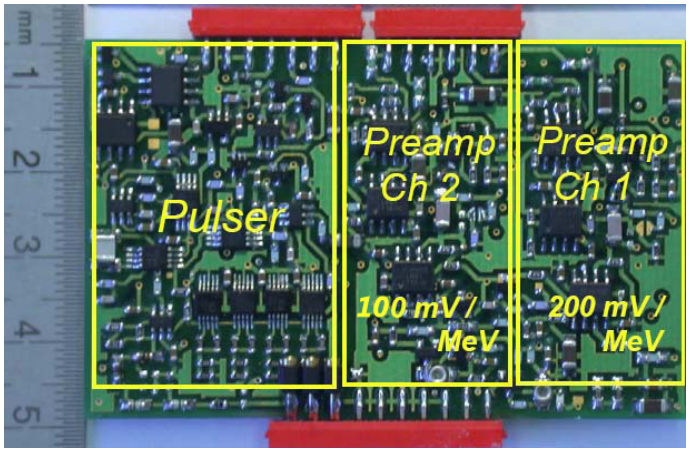

Figure 3.1: Top view of the AGATA core preamplifier. The two different gain channels are indicated on the right. The built-in pulser (left) was used for calibration (taken from [18]).

used in this experiment and indicates the different gain channels implemented on the board of the preamplifier. A crucial component of this new preamplifier is the built-in fast reset circuit. This circuit is part of the second amplifier stage and therefore integrated in both channels.

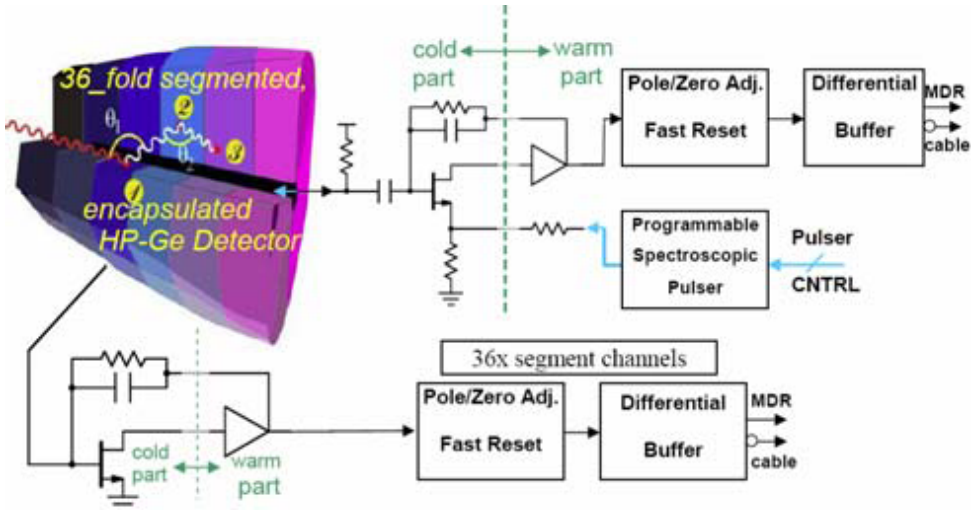

Figure 3.2: Schematic circuit diagram of the detector and the preamplifier electronics: At the top the core with collection stage, fast reset circuit, second amplifier stage and integrated pulser is shown, at the bottom the circuit of one of the segments (taken from [18]).

In figure 3.2 the different parts of the preamplifier are shown schematically. The first amplifier stage is directly attached to the HPGe crystal. This stage is divided into a cold and a warm part. The cold part of the amplifier is operated at about 100 K and therefore located in the cryostat of the detector. The fast reset circuit and the

second amplifier stage, the so called differential buffer, are implemented downstream. The upper part of the figure shows the circuit of the dual gain preamplifier with integrated pulser for on-board calibration purposes, the lower part shows the circuit of one segment exemplarily for all 36 channels. Figure 3.3 shows a block diagram of

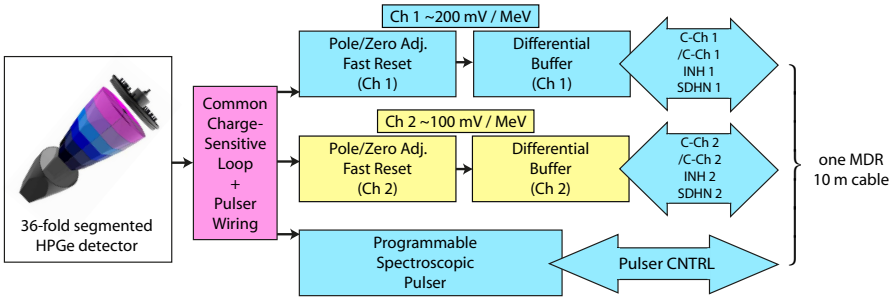

Figure 3.3: Block diagram of the AGATA dual gain preamplifier. Both gain channels share the same charge sensitive loop but have their own fast reset circuits and differential buffers. The pulser affects the common loop directly. '*C-Ch1/2*' are the core channels 1/2, transporting the energy signals, '*INH1/2*' are the inhibit signals of channel 1/2, transporting the block signal, which is discussed later. '*SHDN1/2*' denotes control over the fast reset circuit (adapted from [18]).

the two core channels. Both channels share the same charge sensitive loop followed by two separate fast reset circuits. Downstream the fast reset, there is a separate second amplifier stage for each gain channel with a subsequent output stage. '*C-Ch1/2*' are the core channels 1/2, transporting the energy signals, '*INH1/2*' are the inhibit signals of channel 1/2, transporting the block signal, which is discussed later. '*SHDN1/2*' (short for *shutdown*) denotes control over the fast reset circuit. Usually, the voltage signal of a HPGe detector is characterized by an exponential decay with a decay parameter $\tau \approx 1000\,\mu s$. The '*Pole/Zero Adjustment*' in the second stage reduces the decay parameter τ of the exponential voltage signal from first stage from 1000 µs to only 50 µs. This exponential signal with its slow decay would cause a very long dead time and would result in event pile-ups for multiple energy depositions in the crystal. Therefore, the second amplifier stage includes a fast reset circuit (see figure 3.4). For large energy depositions (i.e. $> 10\,MeV$ for the high gain channel, $> 20\,MeV$ for low gain) the collection capacitance of the second stage gets saturated. The Schmitt trigger's threshold gets exceeded, causing a circuit containing a strong current sink to be connected to the second stage of the preamplifier. This sink is the main component of the fast reset circuit and discharges the saturated capacitance rapidly once activated. When the capacitance is discharged, the Schmitt trigger's lower threshold is passed and the additional circuit containing the current sink

is disconnected. The exponential decay of the signal of the preamplifier is now transformed into a linear decay with a further reduced decay time. Synchronously, the activation of the fast reset via the comparator is given out as a digital signal, the so called inhibit signal.

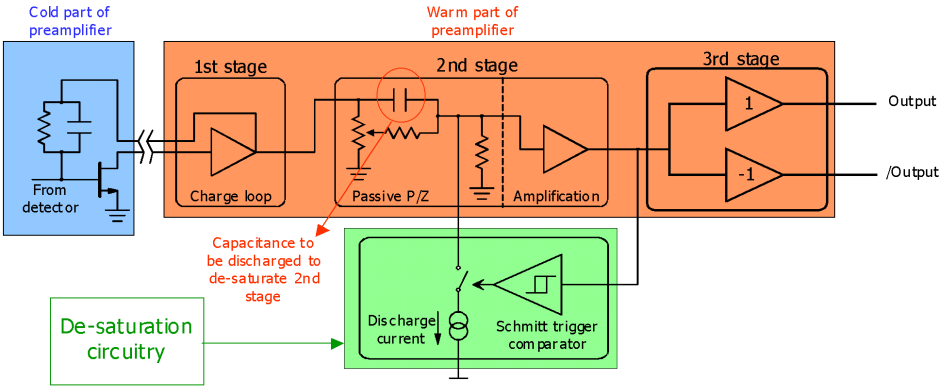

Figure 3.4: Schematic view on the fast reset circuit: For large energy depositions in the crystal the red encircled collection capacitance gets saturated and the Schmitt trigger's threshold is exceeded. The comparator itself closes a circuit and starts a current sink which rapidly discharges the capacitance. After desaturation the lower threshold of the Schmitt trigger is passed and the current sink gets deactivated. The simultaneously created digital signal is transferred as the inhibit output signal (taken from [19]).

Figure 3.5 shows two examples of detector signals, observed with an oscilloscope, using the dual gain preamplifier. In both cases the energy deposition is big enough to saturate the preamplifier of the core electrode, shown in blue. In the example on the left, the fast reset is switched off (SHDN in position off). The saturation of the second amplifier stage leads to a long voltage plateau which then drops off exponentially with decay parameter $\tau = 50\,\mu s$ as mentioned previously. The second energy deposition occurring about 18 µs after the first one in the segment (red signal) cannot be observed in the core signal. Thus, it will not be counted. Effectively, the dead time of the system rises dramatically. On the right hand side, the fast reset is switched on (SHDN in position on). The voltage signal of the segment (red) is similar to the one on the left, showing two energy depositions separated by about 15 µs. The fast reset damps the core signal rapidly as described above. In this example, the complete decay time of the core signal amounts to $t = 10\,\mu s$. Therefore the second (smaller) energy deposition in the segment can be observed and counted in the electronics due to the fast restoration of the core baseline. The preamplifiers are used to date only for the core electrode of the HPGe detector. For

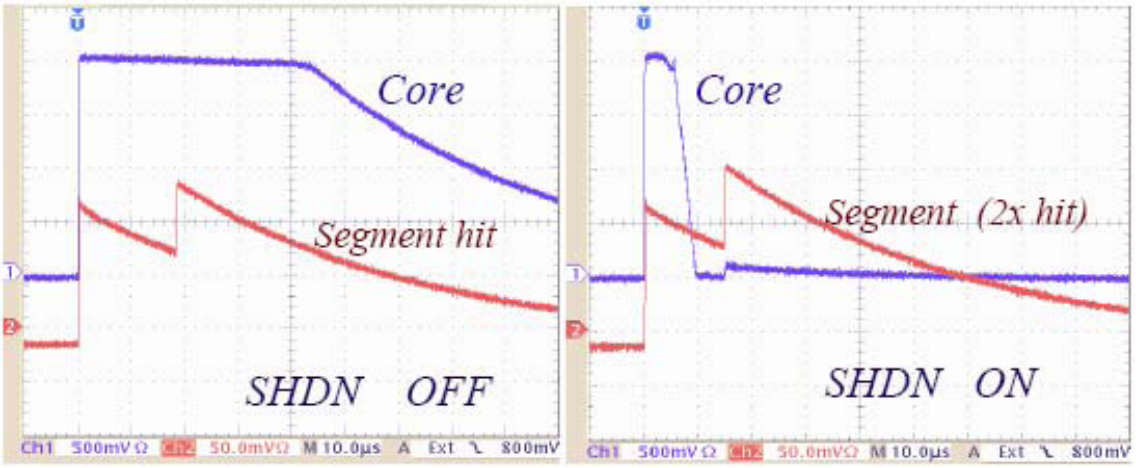

Figure 3.5: Time diagrams of the fast reset circuit: On the left side the fast reset is deactivated. The blue core signal ist plateau-like at the beginning and then drops off exponentially. On the right side the fast reset is activated, the core signal gets strongly damped in a linear way. The second hit in the red segment signal becomes visible (taken from [18]).

a single core preamplifier the gain factor is equal to the lower one on this board, i.e. 100 mV/MeV [18].

3.3 Time over Threshold Method

The fast reset of the core signal allows to use another technique for analysis, the so called *Time over Threshold* method (ToT). The upper diagram of figure 3.6 shows the saturated core signal with the linear decay of the fast reset circuit discussed in section 3.2. In the lower diagram the corresponding digital inhibit signal of the core is displayed. The inhibit signal is generated by the Schmitt trigger. It is a logic signal indicating the activation of the current sink. A positive voltage indicates position ON, whereas no voltage ($V = 0$) means that the current sink is not active (cf. figure 3.6). The length of the inhibit signal is called reset time T. As shown in [23], it is directly connected to the incident energy deposition in the crystal:

$$E = b_1 T + b_2 T^2 - \frac{(V_1 - V_2)}{G} + E_0 \tag{3.1}$$

b_1 and b_2 are time-independent parameters with $b_1 \gg b_2$, V_1 and V_2 denote the baseline before and after the signal (see figure 3.6), E_0 is a general offset term and G is the preamplifier's gain factor. This relation between energy E and T can be used to calibrate the detector in the energy region above the saturation limit of the core signal.

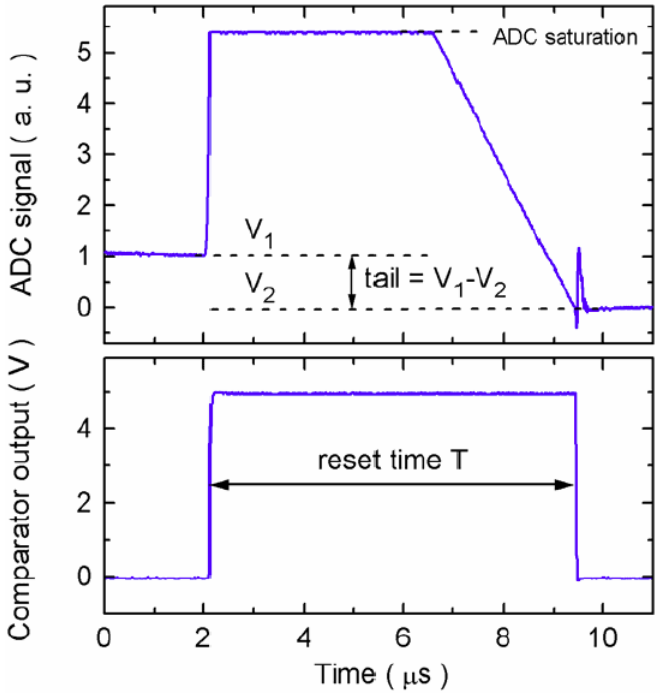

Figure 3.6: The upper signal corresponds to the core electrode signal, the lower one to the inhibit output signal. The inhibit is digital and given out by the Schmitt trigger comparator. It simply denotes the switch positions ON and OFF. The reset time T is the ToT time. Its length is directly dependent on the incident energy deposition in the crystal, see equation 3.1 (taken from [18]).

3.4 Experimental Setup and Electronics

The experimental setup consists of an AGATA HPGe detector and a data acquisition system, i.e. seven converter boxes (see below), ten 'DGF Pixie-4' modules [1] and a dedicated PC for data acquisition and analysis. The output line of the dual gain and the six segment groups (A to F in AGATA notation, [21]) are connected to the converter boxes via seven *Mini Delta Ribbon* (MDR) cables. In these converter boxes the incoming signal lines are split into 2 core energy signals, 2 core inhibit signals and 36 segment energy signals which are then available via BNC outputs. For the segment preamplifiers there is no fast reset implemented. Thus, there are no inhibit signals for the segments. Furthermore, the converters transduce the transfer form of the incoming signals from symmetric differential to asymmetric single-ended. The latter one is much easier to process, even though it is more susceptible to interferences. The converter boxes are connected to *Digital Gamma Finder* (DGF) modules via BNC cables. Every module has four channels, so the 36 segment signals are fed into the first nine modules. The remaining DGF module includes the four

core signals. In the modules the digital *traces* (cf. figure 4.1) of the 40 detector signals are recorded and analysed with a trapezoidal filter with the possibility to obtain MCA spectra. The energy values and traces are then transferred to the PC which writes all events into a file.
Finally, a trigger for data acquisition has to be defined. Here also the fast reset circuit with its Schmitt trigger is useful. The digital inhibit signal generated by the Schmitt trigger can easily be recognised by the DGFs as a start signal. Therefore the electronics record all 40 traces simultaneously if a high-energy event has triggered.
The experimental system was operational from 05/13/11, 3:06 pm to 05/17/11, 2:41 pm with the cryostat standing upright. Thus, the segment ring 1 was the bottommost crystal part. The sector boundary between the sectors A and F was facing roughly towards east.

3.5 Calibration

Due to its high gain factor the so called high gain channel of the core preamplifier gives a very precise measurement of the lower end of the energy spectrum up to an energy of 10 MeV. This allows maximum performance for common γ-ray spectroscopy. At energies higher than 10 MeV the high gain core switches to the ToT mode. The second channel does not switch to the ToT mode until the energy deposited in the HPGe crystal exceeds about 20 MeV. The two gain factors differ by a factor of two and so do the energy ranges. Therefore the low gain channel works linearly in the lower ToT range of the high gain channel (at approx. $10 - 20$ MeV) and can be used for calibration. In figure 3.7 the three methods used for the calibration are shown. The green data points show the calibration via the low gain channel between approx. 10 and 20 MeV. The dashed blue curve represents a fit on data from a pulser calibration performed during the development process of the preamplifier. In the low energy range this pulser calibration matches the low gain calibration very well. Data points in red show the experimentally determined sum of the total energy deposited in all segments of the detector. For this purpose the segment energy information has to be calibrated itself. This was done using an ^{152}Eu source. During this measurement the fast reset circuit was switched off to acquire common MCA spectra for every segment and both core channels. In the analysis four peaks at 334 keV, 778 keV, 964 keV and 1408 keV were used for the calibration. In a first approximation the resulting calibration fit is well described by a linear function. Since the maximum energy deposition of a muon inside a single segment is up to 17 MeV, it is reasonable to expand the linear calibration to this energy. To

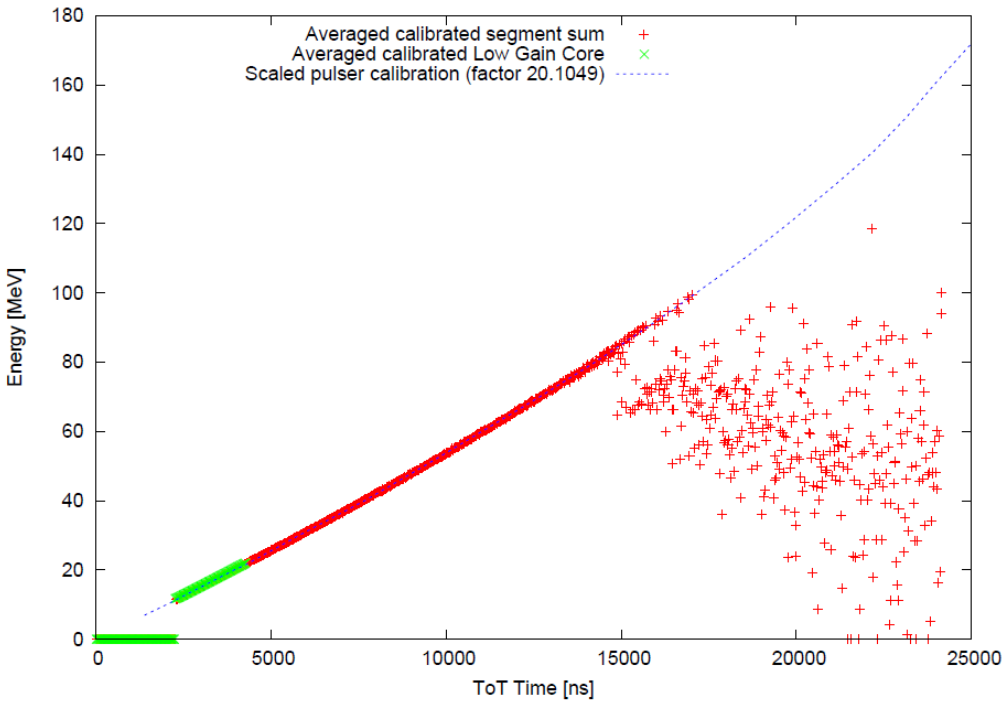

Figure 3.7: Comparison of all three calibration methods: low gain core (green), segment energy sums (red) and built-in pulser (dashed blue). Up to 80 MeV the agreement of the methods is very good. Up to higher energies the segment preamplifiers get saturated and the analysis electronics output too low energy values. Taken from [20].

further reduce the error of the calibration, a calibration source with higher known γ-ray energies has to be used in future investigations. To prove the functionality of the experimental system, the used calibration is more than sufficient. For the calibration of the high gain channel in ToT range the detected energies of a cosmic event in all segments were summed up. Due to various effects discussed below (see section 4.1) this line is not totally clear. Thus, for the upper 90 % of the measured values the average was taken. These averaged energy sums are the data points plotted in red. Up to about 80 MeV they are in very good agreement with the calibration via the low gain channel and with the one performed with the pulser. At about 80 MeV total energy deposition in the detector the red data points start to drop off rather drastically. In this energy regime many segment energies are cut off by the used DGF electronics. Thus, to confirm the pulser calibration above 80 MeV, another experimental method is needed for the future.

4 Analysis of the energy spectra

For the analysis the raw data has to be converted into the *easy list mode*-format (.elm) listing the events as binary words and in uncalibrated channel numbers. Thus, for every event 40 lines exist: 36 for all segments and 4 for the core channels. Every line contains one word for the uncalibrated energy value, one word for the following trace's length (typically 1000 tics with a preset length of 25 ns) and a number of words equal to the trace's length. These last words contain all information about the shape of the detected voltage signal which then can be used to do trace or pulse shape analysis. In fact, the .elm-file is written continuously. For an analysis, which is done event by event, the file has to be preanalysed by a python program. This program produces an ASCII file containing 40 real lines for every event. Every line contains the extracted uncalibrated segment energy, the segment's calibration factor and the trace content. As a second analysis step, the output file is converted into a root-file [6]. The first analysis in [20] was done entirely in python. However, the CERN-based program root covers a wider range of prebuilt tools to analyse the data set. In total 102518 events were recorded.
Firstly, the segment multiplicity of an event and the related energy deposition can be analysed (see section 4.1). By determining the multiplicity, gates can be set in the energy spectra of the segments, sectors and rings. From this, the energy loss and character of the passing particle can be calculated. As a final step, the ring's heights inside the detector can be calculated reversely (see section 4.2).

4.1 Determination of Segment Multiplicity

An essential part in the analysis performed for this thesis is the determination of the multiplicity of an event. In general, the multiplicity of an event is the number of detector segments which are directly affected by incoming particles or radiation. These segments will be called *hit segments* in the following.
As described in section 2.2.1, most of the detected particles in this experiment are assumed to be muons (evidence is given in section 4.2). Contrary to γ-rays, which lose their energy in matter in a limited number of distinctive events, muons

are heavy charged particles, which lose their energy continuously when travelling through matter. Thus, it is necessary to redefine a *hit*, known from the interaction of γ-rays with matter, to the characteristic energy loss of a muon. In a previous work [20] this was done for every event via the recorded traces of each segment. Every trace contains 25 to 30 tics with a length of 25 ns prior to the actual signal which define the baseline. The voltage signal of a hit segment shows a clear rise and then decays exponentially (cf. section 3.2).

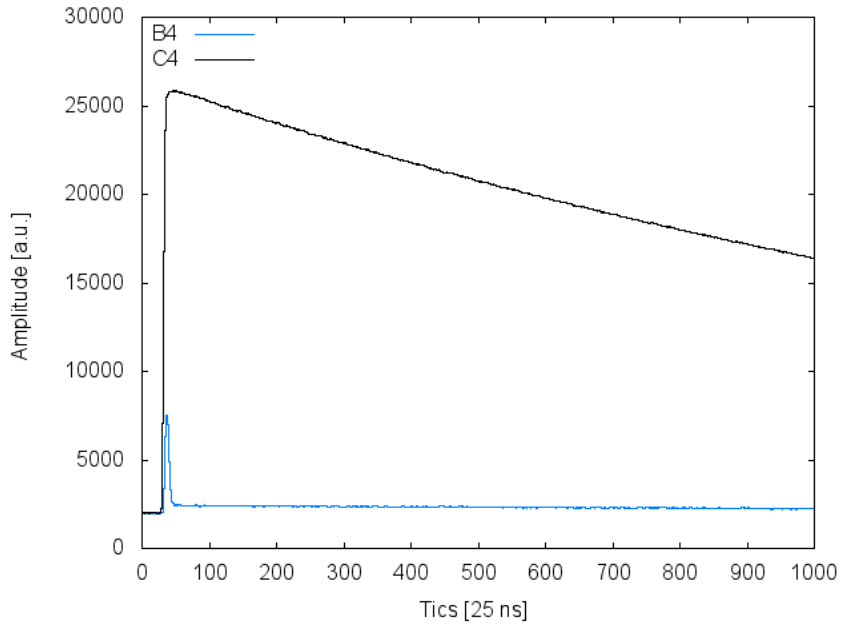

Figure 4.1: Two examples of recorded traces: The black line shows the trace of the *hit* segment C4. The amplitude at the trace's end is clearly more than 6000 ADC units above the leading baseline. The blue line shows the trace of the neighbouring segment B4 and the transient signal connected to the energy deposition in C4.

Even when the DGF's buffer is full (after 1000 tics or 25 µs), such a signal has not come down to the baseline completely. Signals of segments that were not hit have different shapes, depending on various effects, e.g. crosstalk and transient signals, which will be described below. However, the voltage signals caused by these effects will have reached the level of the baseline well before the buffer's end. Therefore it is reasonable to average the first 25 and the last 50 tics and compare those two values. For the measurement in a 64k range the baseline was put to about 2000 ADC units. In a first attempt the two averages, defined above, had to differ by at least 6000 ADC units (on a noise band of typically 50 ADC units) to declare the segment as being hit. However, the following analysis steps showed evidence that a

correction of this hit condition was required. Using equation (2.3), multiplicity can be described as a function of the deposited energy in the detector.

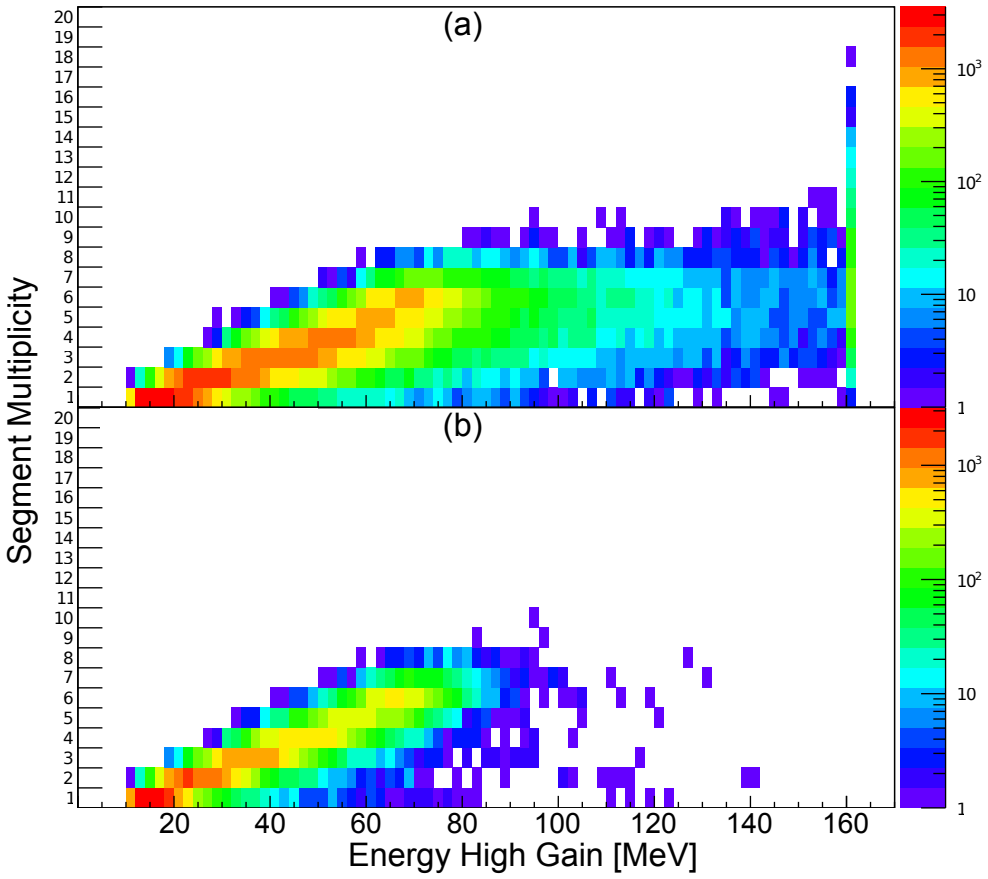

Figure 4.2: (a) Uncorrected matrix plot of multiplicity as a function of energy in the high gain core channel. For energies above 80 MeV the linear trend is not continued. The energy information of the segments contains errors. (b) Corrected matrix plot. Low energy events are preserved well, data points above 80 MeV almost completely vanish. The linear expectation is reproduced.

Due to the finite volume of a segment, increasing energy automatically implies more hit segments. In figure 4.2 multiplicity is plotted as a function of the energy of the high gain channel, which is used in the analysis as a measure for the total energy loss of the muons in the detector. As shown in the upper histogram the distribution of the uncorrected data flattens for energies above 80 MeV. This behaviour can also be observed in the calibration via energy sums as already shown in figure 3.7.
Thus, multiplicity determination depends on the energy registered by the DGF electronics. To investigate this energy dependence, trace contents were compared to the corresponding energy output. It turned out that the trapezoidal filters of the DGFs cannot handle traces with long voltage plateaus. High energy depositions

induce large voltage signals in the preamplifiers and subsequent electronics. For energy depositions exceeding about 17 MeV per segment (cf. figure 4.6), the voltage signals are so large that they saturate the ADC in the DGFs.

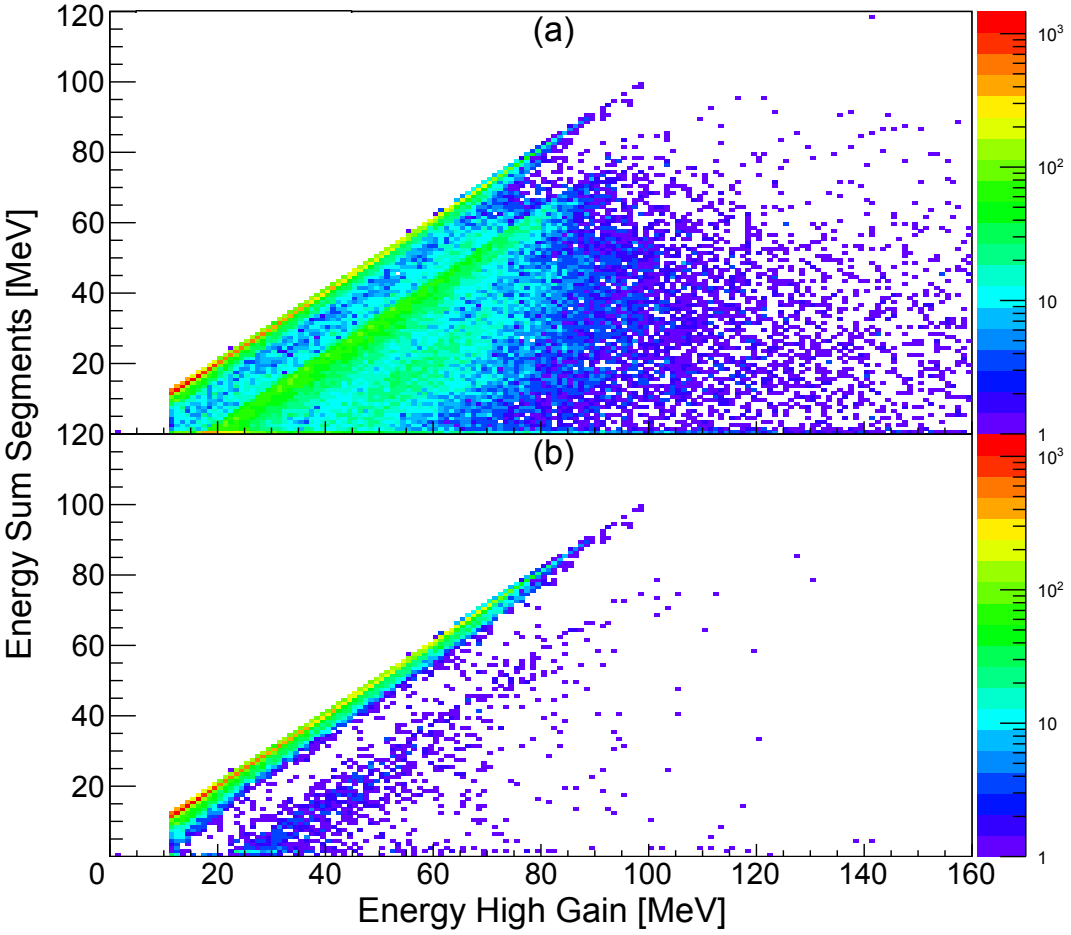

Figure 4.3: (a) Direct energy sum of all segments as a function of the energy in the high gain core channel. Additional to the direct dependency between the energy sums and high gain energy, parallel lines are visible. In these events at least one segment ADC is saturated.
(b) In the corrected data set, the parallel diagonals almost completely vanish. Only physically reasonable events remain for the analysis.

In contrast the AGATA preamplifier of the segment itself is not saturated at the same time. In this case the ADC outputs a signal plateau at the maximum range of 64k. The built-in trapezoidal filter is not able to fit an exponential signal with the preset decay parameter on the trace content. Thus, it returns an energy value of 0 keV. This case is considered in a new hit condition: in addition to the hit determination via trace an energy output of at least 300 keV is required for a hit segment. Moreover, if a segment does not contain this minimum energy, all coincident signals are rejected as well. In the corrected histogram in figure 4.2 almost all data points

above 80 MeV vanish. The remaining data points show a clear linear dependence between multiplicity and deposited energy as expected.
Figure 4.3 shows the energy sum of all segments, plotted against the high gain energy. Again, uncorrected data is shown above and corrected data in the bottom part. In the upper frame the ADC-saturated events are visible as a second (and even third) parallel line to the expected linear energy relation.

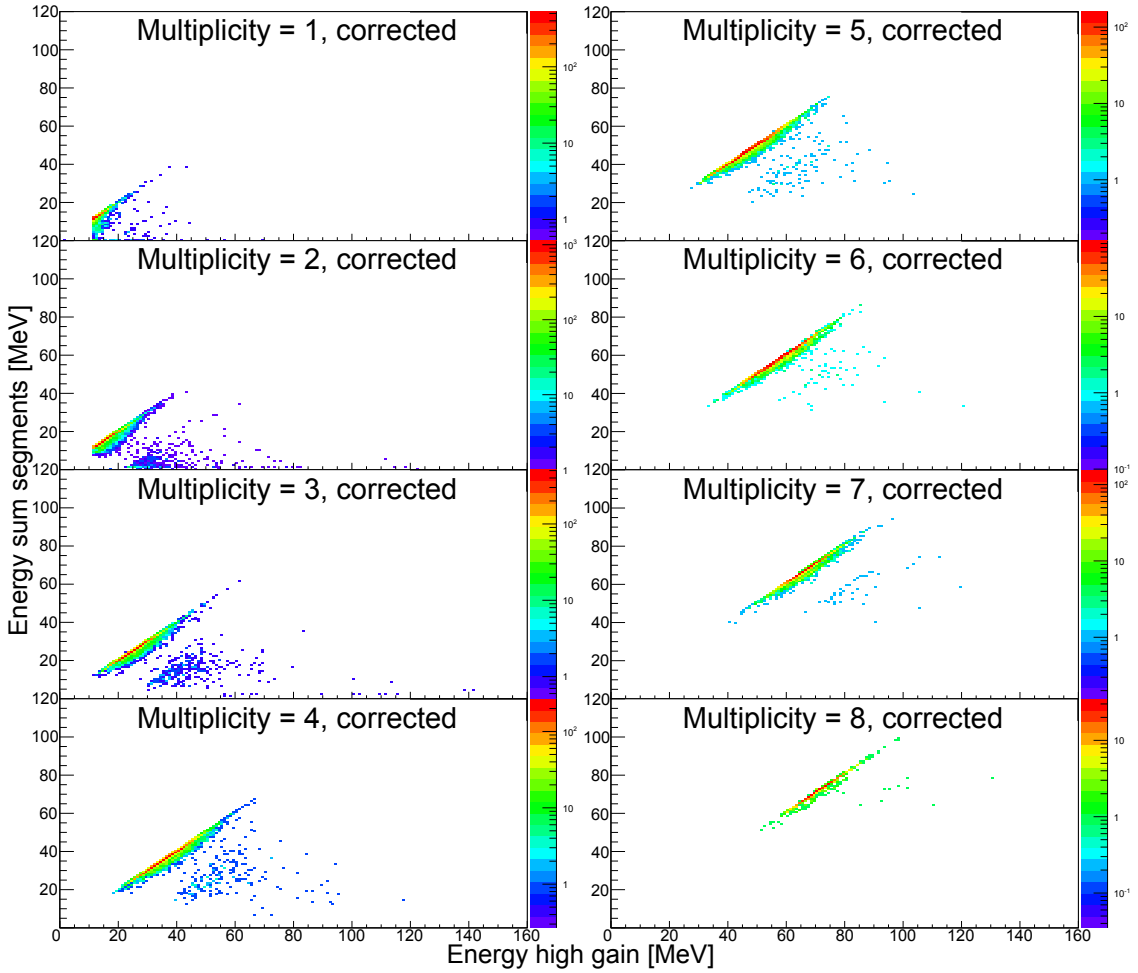

Figure 4.4: Energy sum of all segments as a function of the energy in the high gain core channel, gated on different segment multiplicities. The dependency from figure 4.2 is also confirmed for segment energy sums. The small number of artifacts in the parallel lines only appear at higher core energies and cannot be suppressed by an algorithm.

In general, it is expected that the energy sum of all segments is equal to the energy determined via the core preamplifier. However, if a segment reaches ADC-saturation the output energy is set to zero. Thus, the expected diagonal line is shifted down by multiples of 17 MeV, depending on the number of segments with saturated ADC. In the lower histogram these parallel lines vanish due to the additional required

energy condition. Only a few artifacts and a broadened diagonal line remain, caused by incomplete charge collection in the individual segments. Figure 4.4 shows the same relation but gated for different multiplicities. Like in figure 4.2 increasing multiplicity implies increasing energy values in both the energy sum of the segments and the energy of the high gain channel of the core electrode. Events in the line parallel to the main diagonal only appear at higher energies in each case. These artifacts are not affected by the new hit condition with its energy filter and cannot be suppressed directly. However, their number is very small compared to the events on the main diagonal. The artifacts' influence can be neglected in upcoming analysis steps.

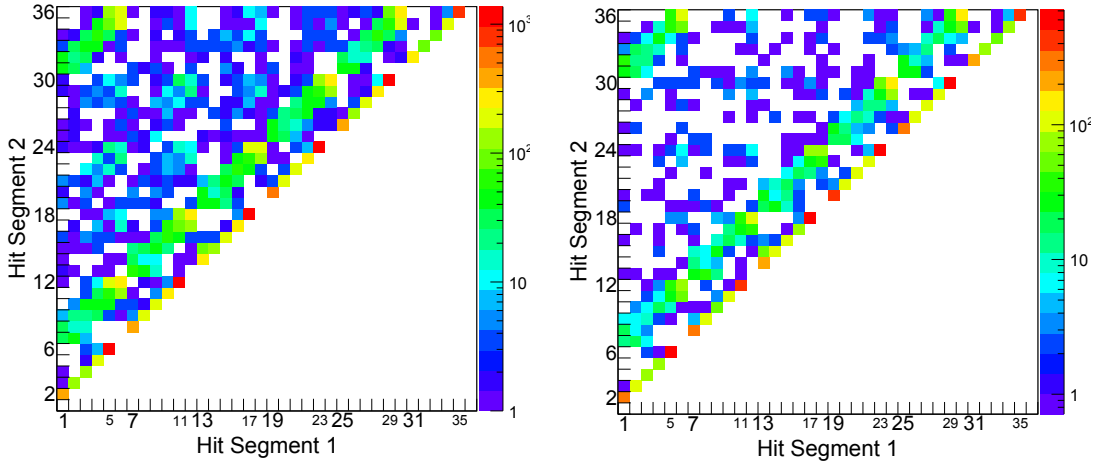

(a) (b)

Figure 4.5: (a) Uncorrected hit correlation for $m = 2$. Entries on the main diagonal describe hits in vertically adjacent segments. The periodical gaps appear due to the detector geometry (see text for details). Entries on the secondary diagonals indicate hits in horizontally or diagonally adjacent segments.
(b) Corrected hit correlation for $m = 2$. Events with a physically not explainable trajectory are strongly suppressed. Statistics on the main and secondary diagonals almost remain constant.

As a consistency check of the new hit condition, the hit correlation between hit segments for multiplicity $m = 2$ is plotted in figure 4.5: the position of one hit segment is plotted against the position of the second hit. Therefore, the 36 segments are numbered consecutively, starting with A1. Thus, B1 is segment 7, etc. Histogram 4.5(a) shows uncorrected data, whereas the histogram in 4.5(b) contains corrected data. The most prominent correlation in both diagrams is the main diagonal starting from $(1, 2)$ to $(35, 36)$. Entries on this diagonal are caused by hits in vertically adjacent segments. Thus, detected particles originate from a source above (or below)

the detector. In the main diagonal periodical gaps are visible, e.g. $(6, 7)$. Entries in these gaps would indicate an event hitting only the topmost segment of one sector and the bottommost segment of a neighbouring sector. Furthermore, the maxima on the main diagonal are directly adjacent to the gaps. Thus, twofold events most likely hit vertically adjacent segments at the top or bottom of the crystal. The combination of gaps and maxima gives a clear hint on the linear trajectory of the detected particles. This is in perfect agreement to the assumption that muons were detected, because to a very good approximation the trajectory of a cosmic muon in the detector is a straight line. Parallel to the main diagonal, two more diagonals can be identified in both diagrams. Entries on these diagonals represent hits in horizontally or diagonally adjacent segments. The maxima belong to hits in two topmost segments, e.g. E6 and F6 in $(30, 36)$. Compared to hits in two bottommost segments this combination is preferred due to the larger size of these segments. As demonstrated in figure 4.5(b), the new hit condition strongly suppresses events with hit combinations of segments not adjacent to each other. To summarize the combination of all the information derived from the diagonals, maxima and gaps provide evidence of linear trajectories through the crystal and therefore back up the muonic character of the detected particles.

4.2 Energy Loss Determination

Minimal-ionizing muons passing matter do not only travel in an approximately straight line, but have characteristic energy losses dependent on the length of the flight path (see figure 2.2). Due to its high segmentation, the AGATA HPGe detector enables the acquisition of energy spectra of different path lengths. With these spectra it is possible to calculate the energy loss per path length and to compare it to literature data for particle identification. Figure 4.6 shows the energy spectra of six different segments. Due to their constant height in the same ring (cf. section 3.1), segments of the same number (X1 to X6 in AGATA notation with $\mathrm{X} = \{\mathrm{A},...,\mathrm{F}\}$) are summed up. Because of ADC saturation the spectra of all six rings are cut off at an energy of 17 MeV, higher energies are set to a value of 0 MeV. As expected from equation 2.3, the peaks are shifted to higher energies for thicker segments (cf. table 4.1) . The high background at lower energies is caused by particles which only hit a corner of the segment but do not cross them in full height. To get a more significant result for the energy loss of the detected particles, the background has to be reduced by gating on specific events.

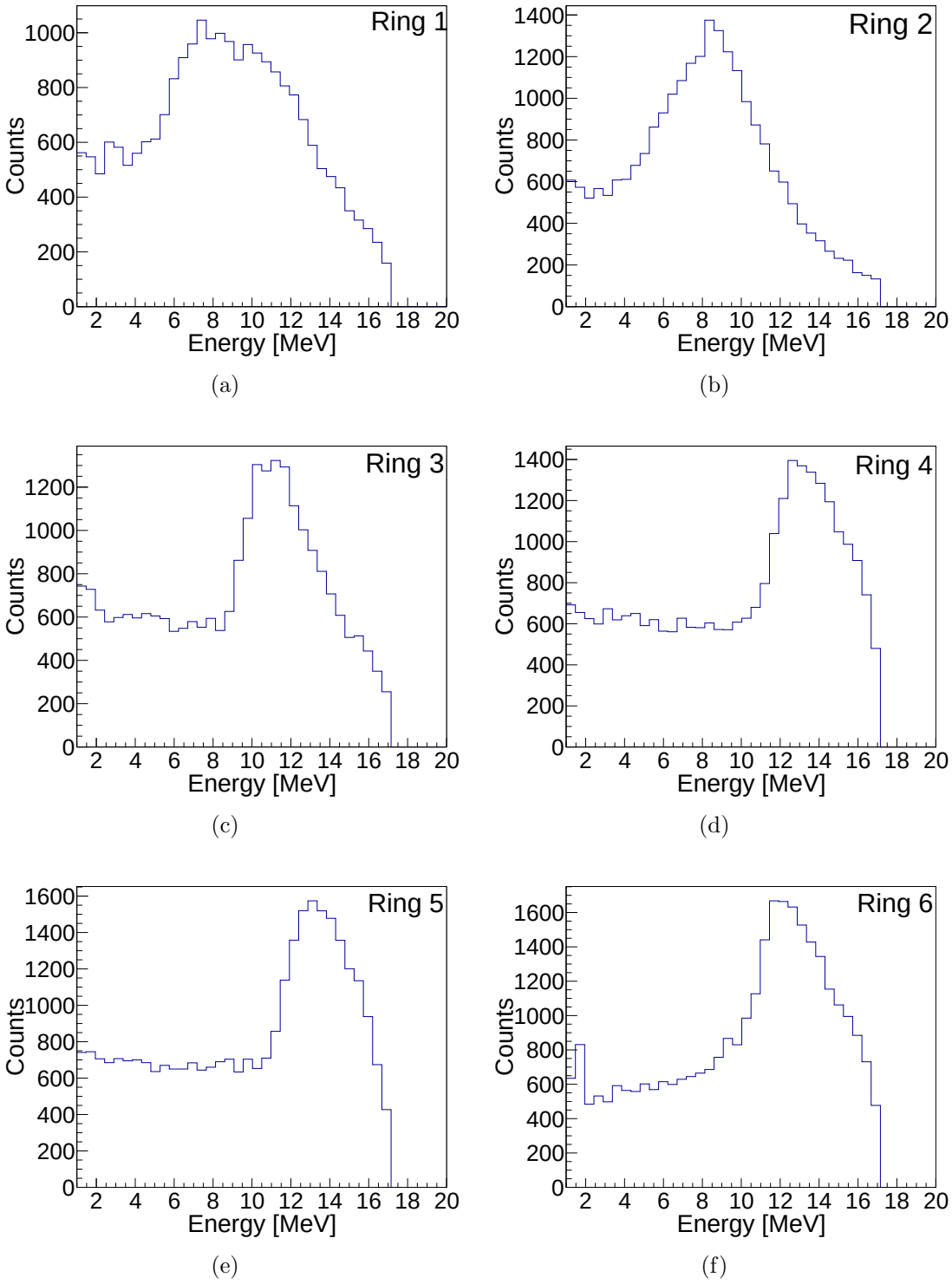

Figure 4.6: Total energy spectra of individual segments. Homonymous segments are combined into the same histogram. At an energy of 17 MeV, the spectra are cut off due to saturation of the ADC. As expected, the peaks are shifted to higher energies with increasing thickness of the segment layer. All spectra are dominated by a continuous background caused by particles, which do not pass the segment in full height, and high-energy background γ-rays.

Table 4.1: Height of the six individual rings in the HPGe detector, taken from [8].

Ring	1	2	3	4	5	6
Height [mm]	8	13	15	18	18	18

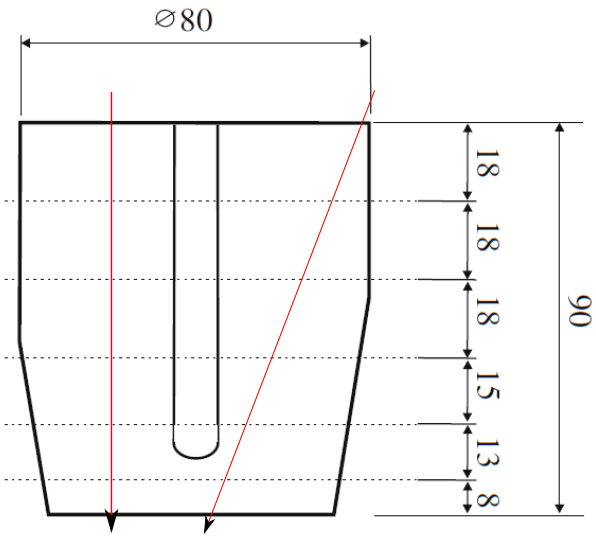

Figure 4.7: Cross section of the crystal. Two extreme trajectories of a particle in a *vertical hit* are shown in red lines. The numbers indicate the dimensions of the crystal and segment heights in mm (adapted from [8]).

For this purpose, particle trajectories from the top to the bottom of the detector are suited best. Furthermore, these trajectories should be as vertical as possible to reduce the deviation of the path length through the crystal. In the following analysis a *vertical hit* in the detector is described by a trajectory with multiplicity $m = 6$ hitting only segments of one sector. Figure 4.7 shows two possible trajectories of a vertical hit with minimal and maximal path length.

The path length has to be known for the determination of the energy loss. Equation 2.3 can be written in a simplified form, only depending on observables within this study:

$$\frac{dE}{dx} \simeq \frac{\Delta E}{\Delta x} = \frac{E_{\text{deposited}}}{s \cdot \rho} \tag{4.1}$$

$E_{\text{deposited}}$ is the energy deposited along the path length s in germanium of density $\rho = 5.323\,\text{g}\,\text{cm}^2$ and can be extracted directly from the energy spectra. Figure 4.8 shows the energy spectra of the high gain core channel. The upper histogram contains the complete ungated spectrum after correction. To obtain the lower spectrum an event gate was set on vertical hits.

Deviations from the mean value of the measured energy distribution are not caused by statistical fluctuations as for the linewidth in γ-ray spectroscopy, but by a con-

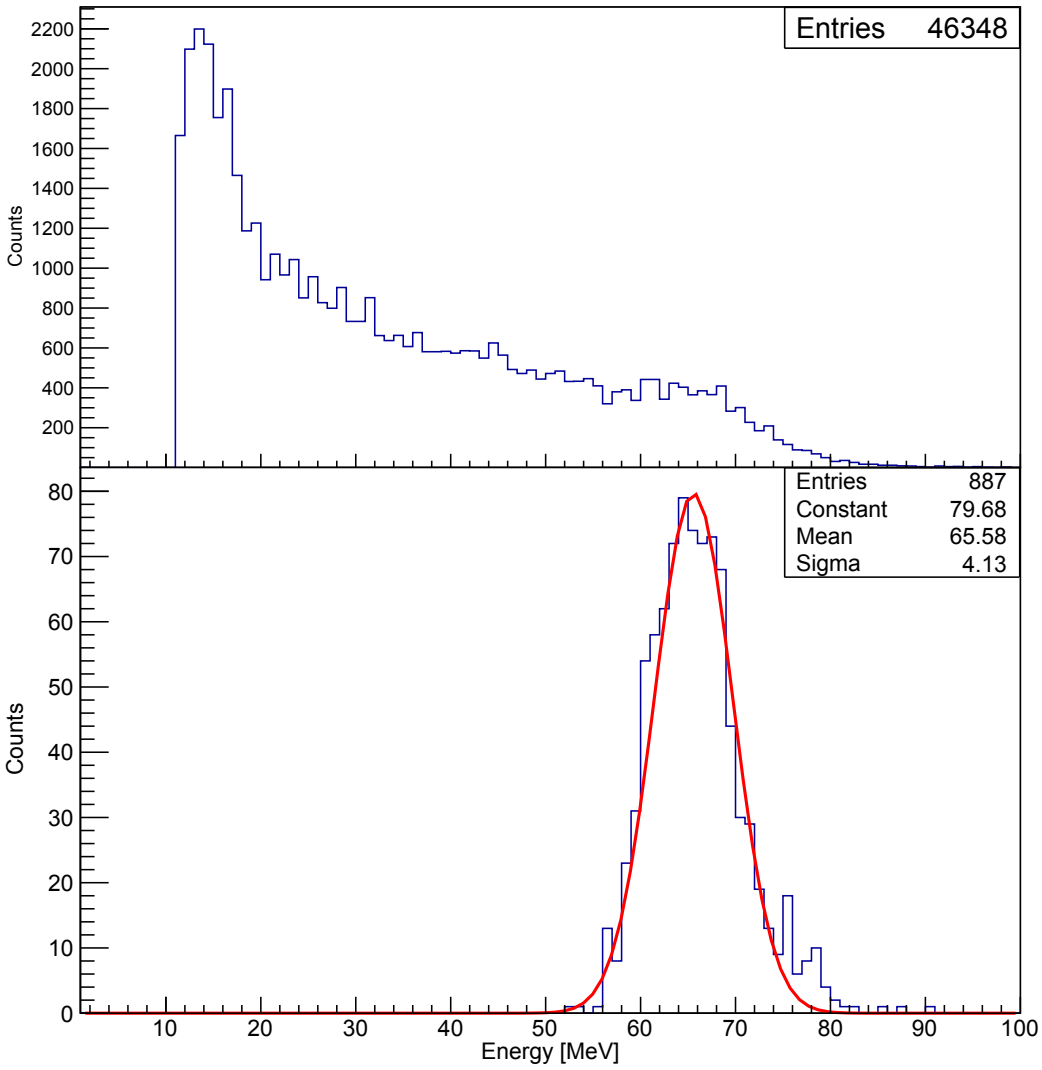

Figure 4.8: Energy spectra of the high gain core channel. The upper histogram shows the corrected, yet ungated spectrum. For the lower diagram a gate on vertical hits is set. The remaining peak is fitted with a Gaussian distribution to obtain a value for the deposited energy in order to calculate the stopping power via equation 4.1.

tinuous energy loss along a path of varying length. Thus, the histogram should be fitted with a Landau distribution as described in [15, 22]. Since the path lengths vary between two extremes, as shown in 4.7, a multiple Landau fit has to be applied. In a good approximation, this multiple Landau fit can be replaced by a simple Gaussian fit, which gives a peak position of 65.58 MeV. Applying this value to equation (4.1) a mean energy loss of

$$\frac{dE_{\text{exp}}}{dx} = 1.37(9)\,\text{MeV}$$

can be deduced. According to [14], the energy loss of minimal ionizing muons in germanium accounts to

$$\frac{dE_{\mathrm{min,lit}}}{dx} = 1.37\,\mathrm{MeV}$$

Thus, gating on top-down events provides strong evidence for the muonic character of the incoming particles. Accordingly, it is possible to reversely calculate the height of the segment rings, taking into account the calculated value of the energy loss.
By applying the vertical hit condition on the energy spectra of the individual rings from figure 4.6, the gated spectra in figure 4.9 are produced. In all six spectra, the low energy background is suppressed completely. Only the spectrum of ring 6 shows a low energy tail for the peak at 11.59 MeV. This tail and the broadened distribution in the spectrum of ring 1 have a common cause: Vertical hits do not necessarily penetrate the topmost (ring 6) and bottommost (ring 1) segment in full height, but can enter or leave the segment at the vertical sides. Therefore, it is neither possible to fit the spectrum of ring 1 nor to get physically reasonable fit parameters from it. Following equation 4.1, a shorter path length subsequently implies less energy deposition in the detector. Thus, the peak energy can be identified as the energy loss of a muon traversing the particular segment vertically on the shortest path (cf. figure 4.7 on the left side).

Table 4.2: By fitting the peaks from the spectra in figure 4.9 the mean energies can be used to calculate the segment heights via equation 4.1. The specification values are taken from [8].

Ring #	peak energy [MeV]	calculated ring height [cm]	specification [cm]
1	n/a	n/a	0.80(8)
2	7.9(21)	1.08(29)	1.30(13)
3	10.1(6)	1.38(12)	1.50(15)
4	12.3(7)	1.69(15)	1.80(18)
5	12.5(8)	1.72(16)	1.80(18)
6	11.6(6)	*1.59(13)*	*1.80(18)*

Table 4.2 shows the fit results for the spectra in figure 4.9. The thicknesses of the different rings were calculated by applying the peak energies to equation 4.1. For rings 2 to 5 the specification values (taken from [8]) were reproduced by the reverse calculation within the error. Nevertheless, there is a systematical error which forces all calculated height values to be a little to low. Despite this systematical error, the ring height of ring 6 is clearly to small as indicated by the italic numbers. Since the peak shape is not distorted in respect to a Landau distribution, the deviation of the expected mean energy can only be caused by a ring height which is essentially

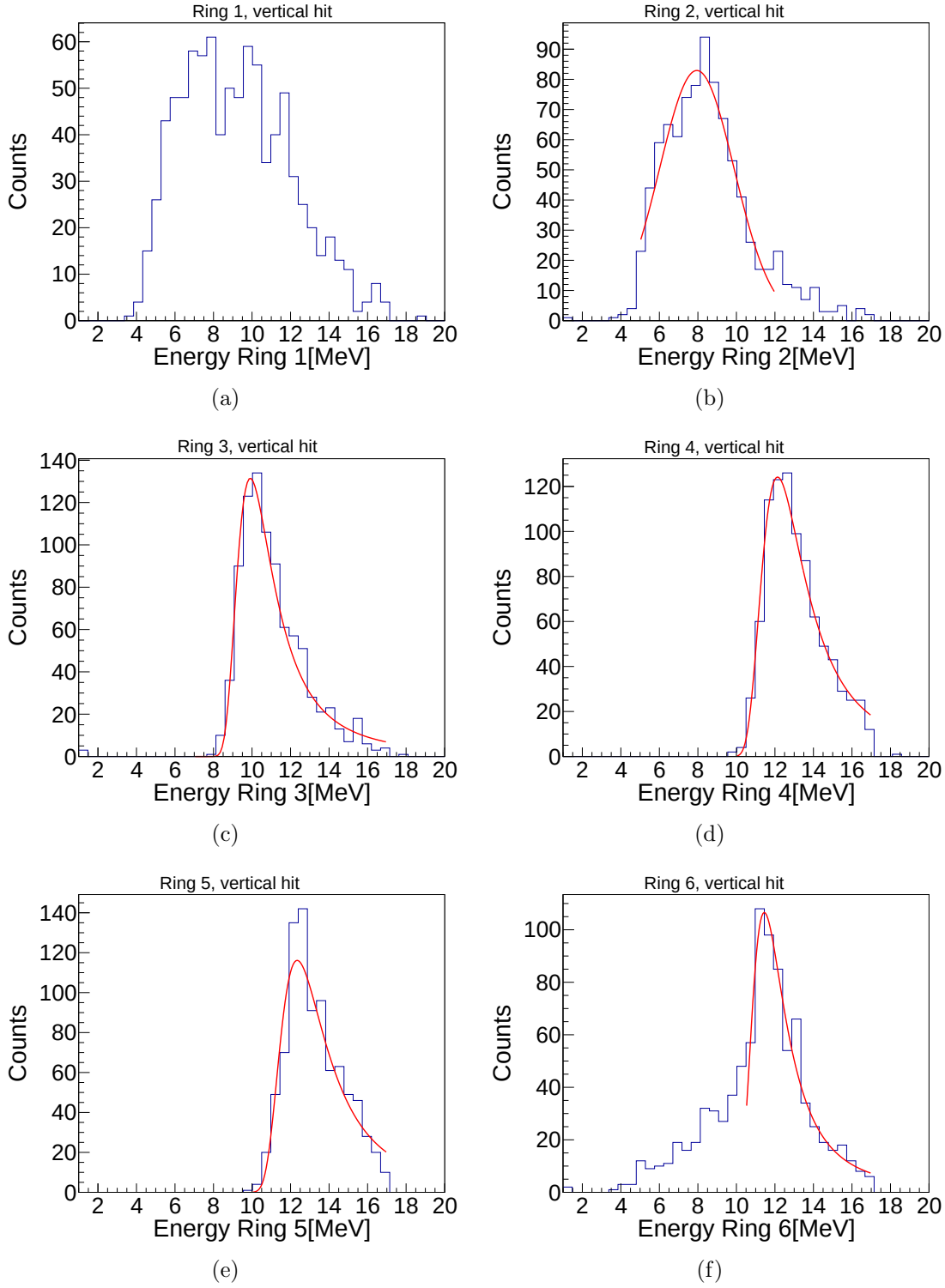

Figure 4.9: The energy spectra for the different rings from figure 4.6 are gated by the *vertical hit* condition. The low energy background is clearly reduced or completely suppressed. The spectra of rings 2 to 6 can be fitted by a Landau distribution to obtain the energy loss in the particular ring. The low energy tail of ring 6 and the broadened distribution of ring 1 can be explained by trajectories which do not pass these edge segments in full height but enter or leave at the segment's side.

smaller than specified. In the height specifications given in [8], a crucial part of the crystal construction is not taken into account: the intrinsic surface of such a detector consists of an electrically neutral passivation layer to avoid leakage currents.

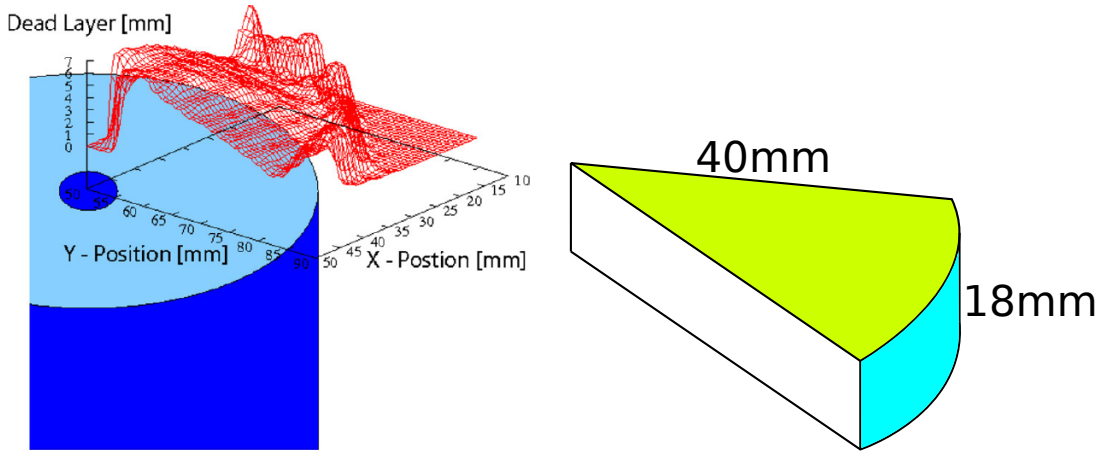

(a) (b)

Figure 4.10: (a) The intrinsic surface of an AGATA HPGe crystal consists of an electrically neutral passivation layer (dead layer). The width of this layer was determined first by Eberth and Simpson. Accordingly, the passivation layer extends from $1-2\,\mathrm{mm}$ at the outer surface to $5-7\,\mathrm{mm}$ at the inner core contact (taken from [9]).
(b) Sketch of a single segment in ring 6. The area of the two coloured surfaces is used to calculate the amount of background in figure 4.11. The intrinsic surface is coloured green, the lateral surface blue.

Figure 4.10(a) shows the results of a measurement on a similar detector performed by Eberth and Simpson [9] employing a detector scan with a ^{241}Am source in order to determine the width of this passivation layer. Accordingly, the passivation layer extends from $1-2\,\mathrm{mm}$ at the outer surface to $5-7\,\mathrm{mm}$ at the inner core contact. By comparing the energy deposition in ring 6 to the energy depositions in ring 4 and 5 respectively, it is possible to calculate the width of the apparent dead layer. Since the energy loss of minimal ionizing heavy particles is proportional to their path length in the detector, the calculation of the width of the dead layer for ring 6 is simply geometrical. According to the specified layout of the detector, the rings 4 to 6 should be equally high. Thus, the ratio of the detected energies in ring 6 to ring 4 or 5 is proportional to the dimensions of the active layer in ring 6:

$$h_{\text{dead layer}} = 18\,\mathrm{mm}\left(1-\frac{E_6}{E_i}\right) \qquad i=4,5 \tag{4.2}$$

The determination of the dead layer width is performed for each vertical event. Figure 4.11 shows the results of this calculation. The comparison of the energies of ring 4 and 6 is shown in red, the comparison of ring 5 and 6 in black. Both calculations show comparable results and the method seems to work successfully. The form of the spectrum follows the expected trend. As the circumference of a circle gets larger for increasing radii, more hits should be registered in the outer parts of the detector. In comparison to the results of Eberth and Simpson [9], larger values for the width of the dead layer are calculated in this experiment. The

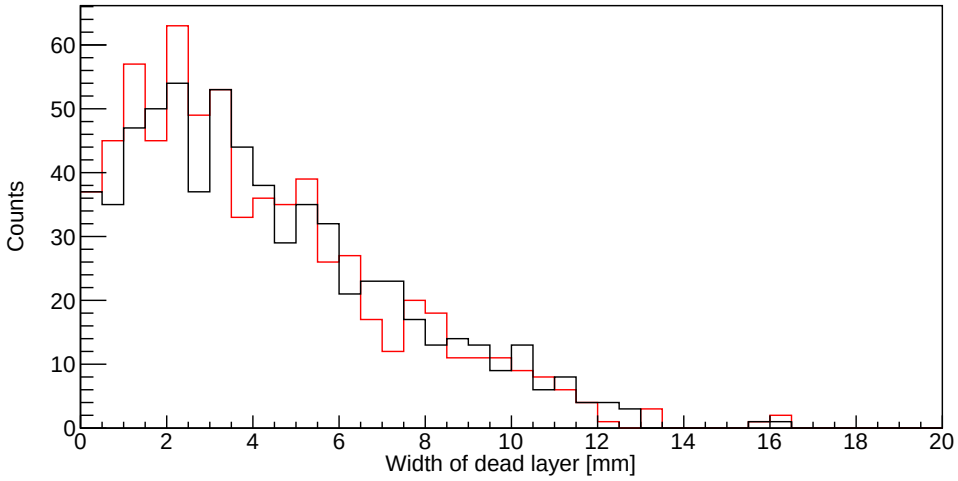

Figure 4.11: The inactive passivation layer at the intrinsic surface of the detector can be calculated by comparing the energy deposition in ring 6 to the energy depositions in ring 4 (red) or 5 (black). Both methods show comparable results. The measurements performed by Eberth and Simpson [9] can be confirmed.

difference consists in the determination of a vertical hit for the calculation method. As already stated in the discussion of figure 4.9(f), particle trajectories can enter or leave the outermost segments at the side and are still counted as a hit. As the energy deposition of such a hit in ring 6 is lower as well, these lateral hits produce a background below the distribution. Due to the linear dependency of the energy loss on the path length, the background is distributed uniformly. It is apparent that background contributions above 13 mm are missing. The energy deposition of such an event in ring 6 is not high enough to consider the segment as being hit. Therefore, these events are rejected as a vertical hit.
Figure 4.10(b) shows a sketch of a single segment in ring 6. To determine the amount

of background in the spectrum in figure 4.11 the areas of both the intrinsic surface (green) and the lateral surface (blue) are compared geometrically:

$$\frac{A_{\text{lateral}}}{A_{\text{lateral}} + A_{\text{intrinsic}}} = 0.459 \pm 0.018$$

Thus, the spectrum would have to be reduced by a uniform background with an integral of almost half of total statistics. However, the general conclusion regarding the spectrum does not change. In fact, the background correction would eliminate larger values and the results by Eberth and Simpson can be verified.

5 Tracking of muon trajectories

Tracking a muon's trajectory through the crystal requires three spacial coordinates in the detector's reference system. Since the energy deposition is linear and continuous, the vertical *height* information is given by the preliminary tracking via segment hits performed in section 4.1. As the detector is approximately cylindrical, the introduction of a cylindrical coordinate system is reasonable. However, the angular information has to be determined individually for each hit segment with respect to its segment boundaries and not as an angle depending on a preset reference point (see section 5.1). The radial information will be analysed by evaluating the rise time of the voltage signal of the hit segments (see section 5.2).

5.1 Lateral Tracking

High-energy muons penetrate matter on a straight path. In the previous chapter, only a preliminary tracking by whole hit segments was accomplished. For a more precise determination of a muon's trajectory through the crystal, the transient signals in segments not directly affected by the particles may be analysed. In contrast to γ-ray spectroscopy, the interaction of the particles in the crystal is not point-like but linearly extended. Thus, the *Pulse Shape Analysis* (PSA, [8]) of the AGATA community cannot be applied. Instead, the segment traces have to be analysed by a new method.

As mentioned before, the trace of a hit segment shows a steep voltage rise and a slow exponential decay (cf. figure 4.1). Additionally, figure 5.1 shows the traces of segments horizontally adjacent to a hit segment. Segment E4, illustrated in black, clearly is hit. The traces of segments D4 (blue) and F4 (red) feature smaller voltage bumps. The rather short *transient signals* are induced by the passing muon which creates large charge separations in segment D4 via its energy loss. Following electrodynamics, a larger voltage signal implies either a larger inducing charge or a smaller distance to that charge. By comparing two transient signals on opposite sides of the hit segment, only the distances to the inducing charge are of interest as the amount of charge is equal for both transients. Thus, it is reasonable to define

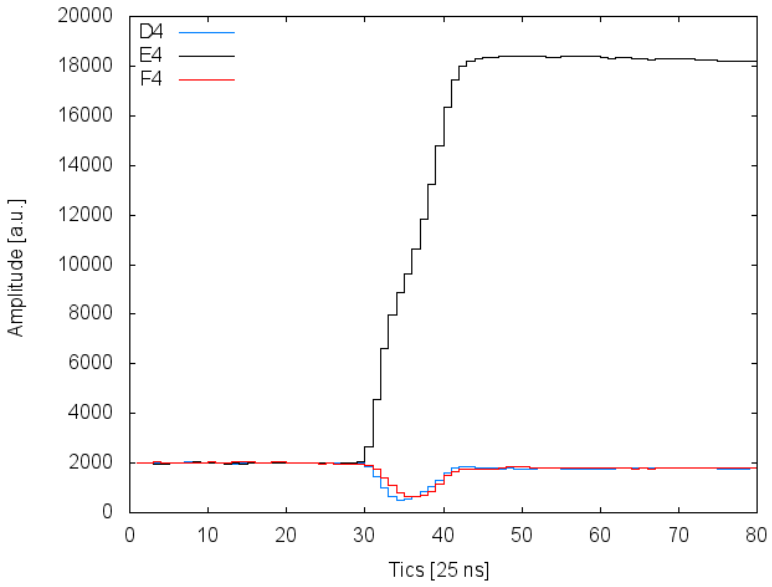

Figure 5.1: The black line shows the trace of the hit segment E4 (black). The time frame is limited to the first 80 tics. The traces of the horizontally adjacent segments D4 (blue) and F4 (red) show clear *transient signals*. Their height is used to determine the position of the muon's trajectory in respect to the hit segment's boundaries. A radial information cannot be extracted from neighbouring segments.

a *weighting factor* which defines the position of the interaction in respect to the segment boundaries:

$$\zeta = \frac{h_{\text{right}}}{h_{\text{left}} + h_{\text{right}}} \tag{5.1}$$

The observable h denotes the height of the transients, the indices stand for the position of the segment recording the transient in respect to the hit segment. Since transients can also be negative, the height values have to be absolute values. A C++ program calculates the transient heights iteratively. The algorithm determines a maximum value in the first 50 tics and averages a baseline after that. The difference between these two values results in the transient height. The position index is defined in absolute terms for the used experimental setup to enhance the presentability of the calculated tracks later on. Thus, segments with a transient signal in the position 'right' are located on the right side of a hit segment if viewed in the actual experimental system, segments in the position 'left' respectively.
The weighting factor is defined in the same way: events with $\zeta = 0.5$ deposit their energy in the middle of the intersegmental boundaries. A weighting factor of $\zeta < 0.5$ denotes trajectories in the left half of the segment, $\zeta > 0.5$, respectively, in the right half. Figure 5.2 shows six exemplary spectra of weighting factors for the

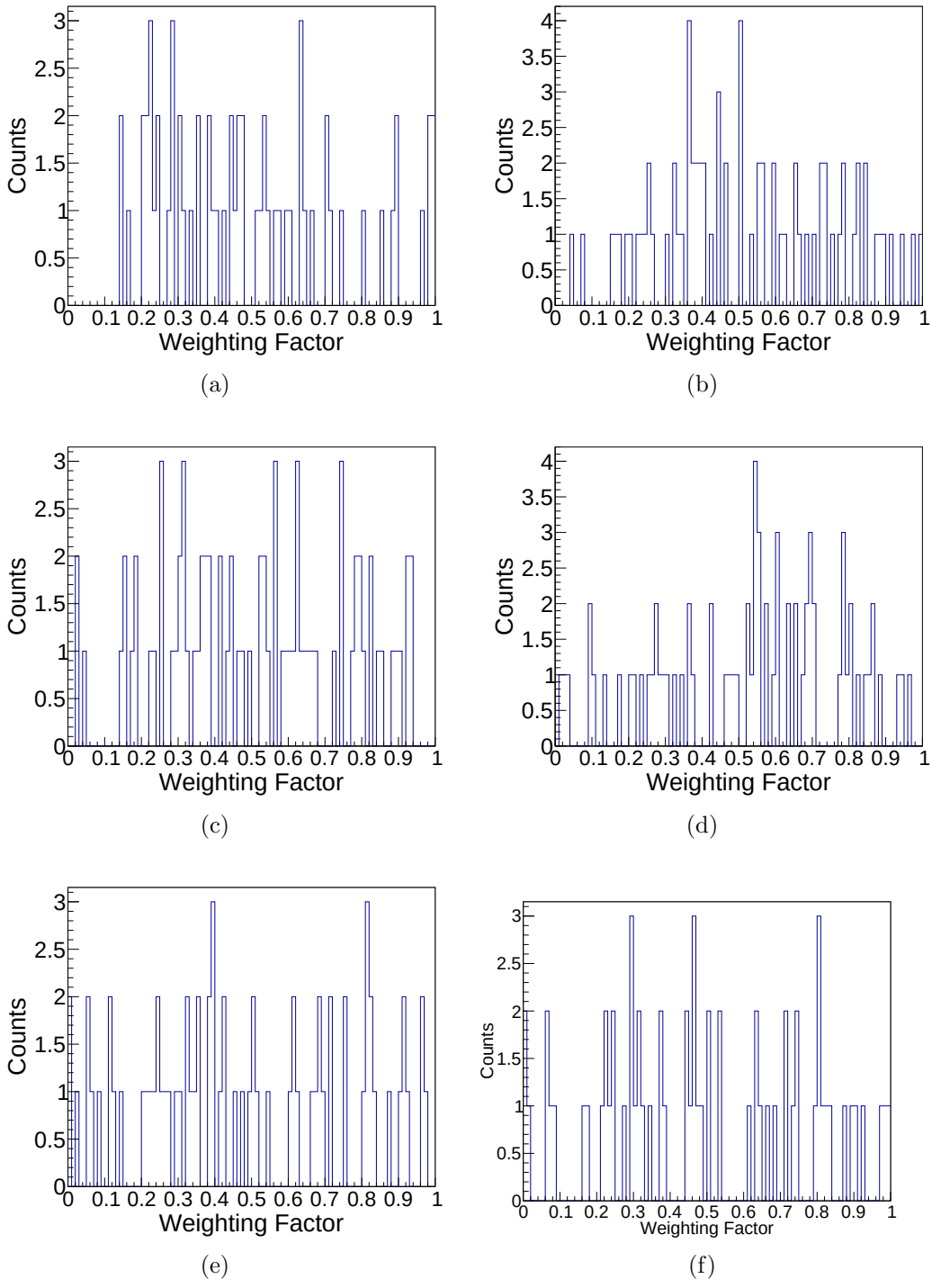

Figure 5.2: Examples of weighting factors for vertical hits for the six segments in sector A. The *weighting factor* describes the relation between the height of the two transient signals neighbouring an energy deposition. As expected, the spectra are uniformly distributed.

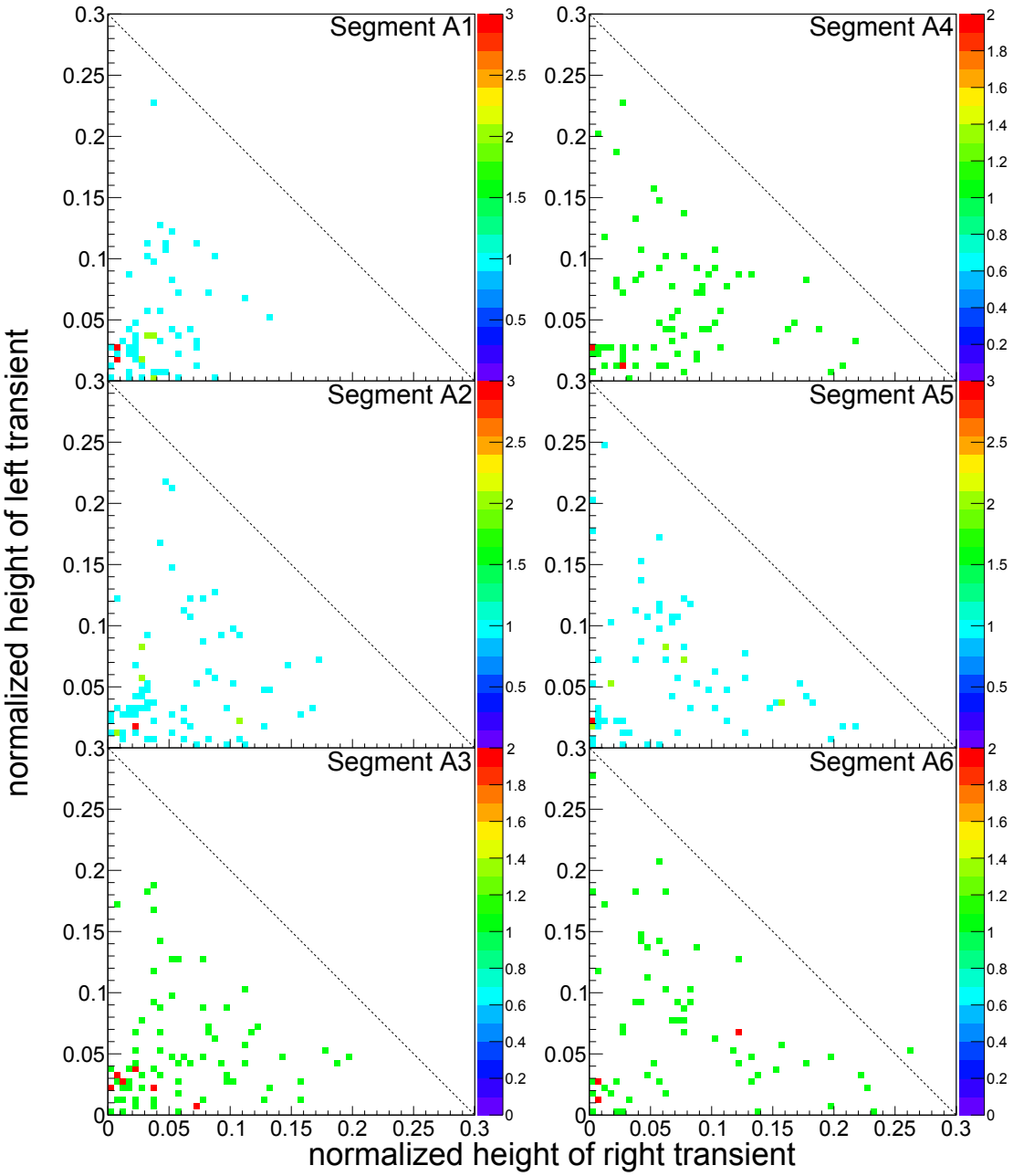

Figure 5.3: Correlation plots of the normalised height of two associated transients. By expectation, all data points should be on a thought diagonal. Instead, all data points seem to be randomly distributed below such a diagonal. From this, a first hint on the radial component can be won.

whole sector A. As this analysis algorithm is the easiest, a gate was set on vertical hits to verify the method. Since the weighting factor makes no predication about the radial information, i.e. the distance of the trajectory to the core or outer electrode, there should be no predominant features in the spectra of the weighting factor. As expected, the spectra in figure 5.2 are uniformly distributed. The spectra of the 5 remaining sectors show the same behaviour.

To verify the lateral tracking method via weighting factors, the two associated transient heights can be plotted against each other. Figure 5.3 shows the plots for vertical hits in sector A. The transient heights are normalized by the signal height from the hit segment's trace. By expectation, one transient should get smaller in the same amount the second transient gets larger. Thus, all data points should be located on a thought diagonal line which connects same axis values. In fact, all data points (for all segments) are distributed below such a diagonal. This can be interpreted by introducing the radial component discussed in section 5.2. Since the detector shape is rotationally symmetric, charge clouds in outer parts of a segment produce different transient heights than charge clouds in inner parts near the core electrode. Due to bigger distances to neighbouring segments, especially the transient height differences increase strongly for increasing radii. Thus, gating on increasing distances to the core electrode should result in diagonal lines of data points, increasingly shifting to the dashed line plotted in figure 5.3.

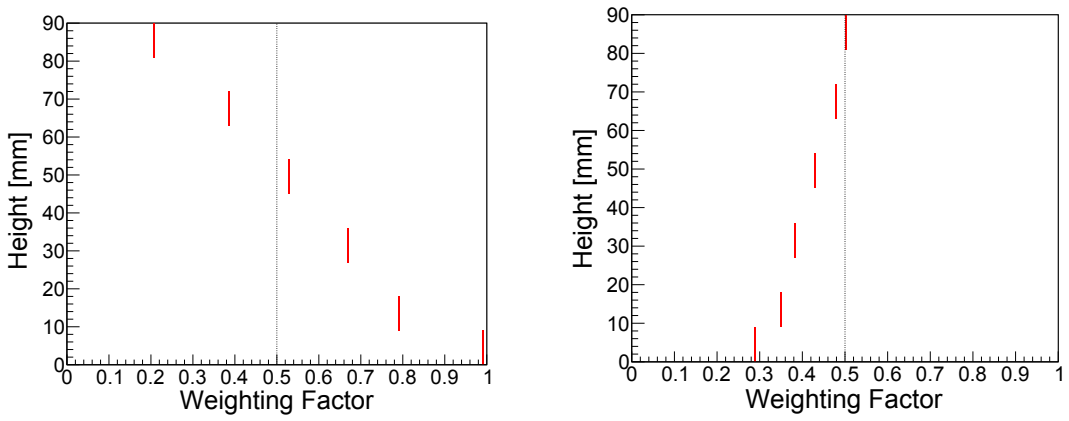

(a) (b)

Figure 5.4: Two examples of laterally tracked muon trajectories in a vertical hit. The six weighting factors of the same event in sector A were combined into one diagram. The vertical axis approximately describes the position in height of the individual segments. The vertical dashed line at $\zeta = 0.5$ marks the lateral middle of the segments and only exists for reasons of orientation. As expected, both tracked trajectories show a linear trend.

For tracking purposes, the single weighting factors of an event have to be combined. Figure 5.4 shows two examples of reconstructed muon trajectories from a vertical hit in sector A. The gating on vertical hits was chosen only for reasons of presentability. As the weighting factor is defined as a projection on the detector surface, the diagrams can be considered as a direct view on the detector. Thus, the trajectory in figure 5.4(a) runs from the top left to the bottom right inside sector A, i.e. clockwise if viewed from segment A1. The trajectory in figure 5.4(b) starts in the middle of A6 and runs straight to a more sinistral position in segment A1. This tracking method was performed successfully for the first 80 of 887 vertical events. The remaining events still have to be analysed. Due to the merely relative character of the weighting factor, the radial position of the individual segment interactions has to be determined to complete the tracking algorithm.

5.2 Radial Tracking

The radial coordinate of an energy deposition inside a certain segment can be determined via the *rise time* of the trace of this event.

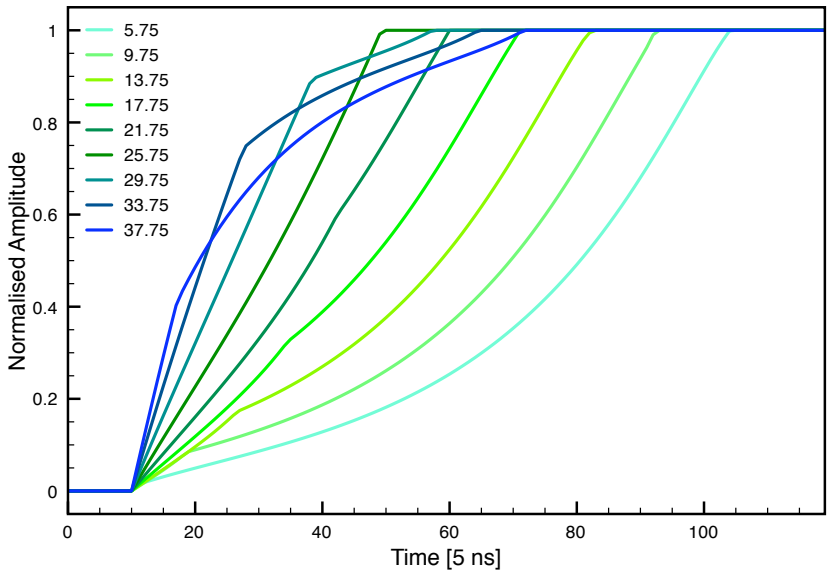

Figure 5.5: Simulated traces of a hit segment for different radii as used by the AGATA community. Due to the different mobility of electrons and holes in the germanium volume, rise times vary with different distances between the interaction point and the core electrode. Due to a low time resolution by the DGFs, the kinks in the rising part of the traces, which are important for PSA, are not visible in the performed experiment. Taken from [5].

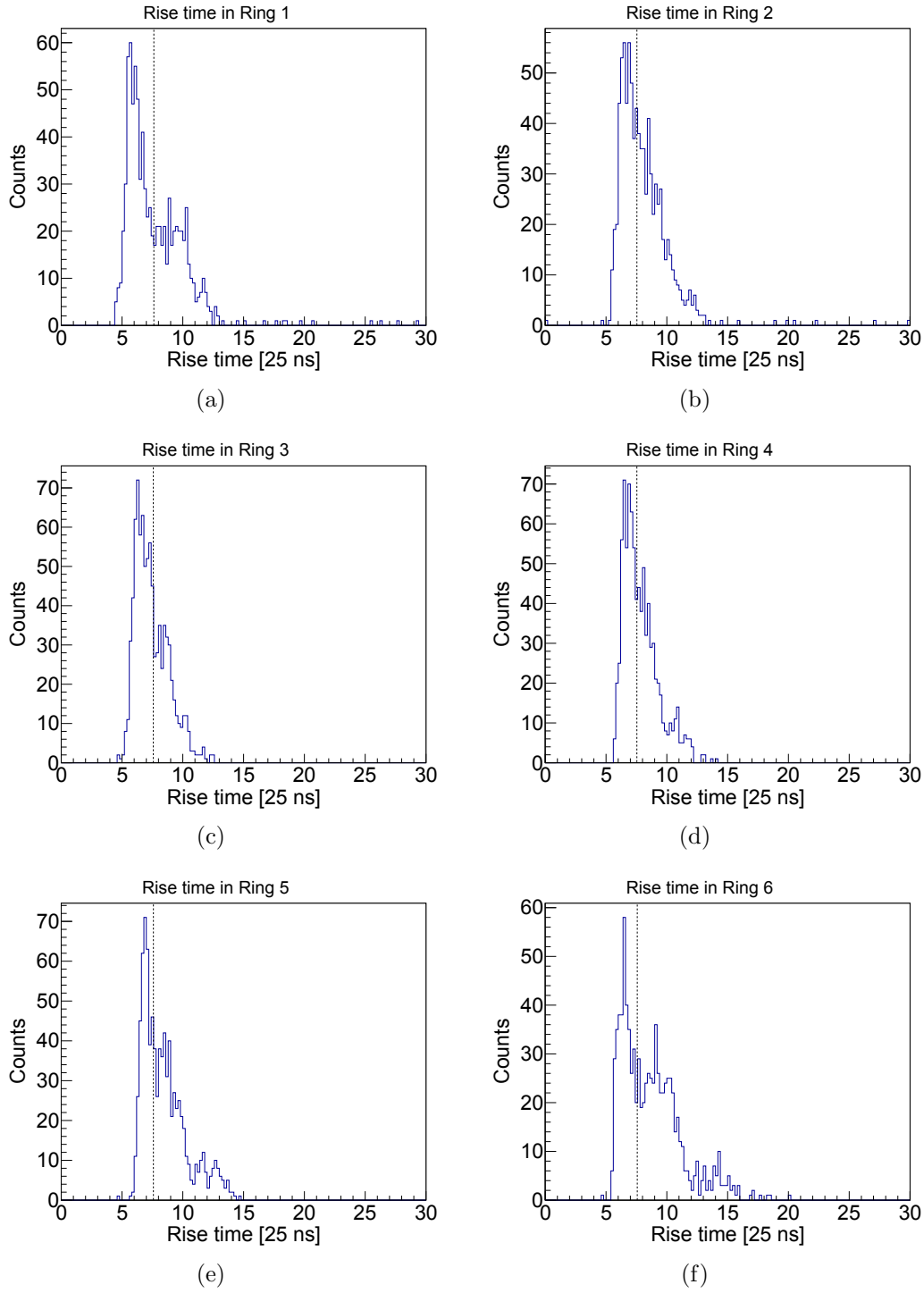

Figure 5.6: Rise time spectra for all rings, obtained by gating on vertical hits. The vertical line describes a lower limit for radially space resolved tracking. Rise times below this limit cannot be assigned unambiguously. Thus, hits in the outer part of the crystal can only be distinguished in their lateral coordinate.

Figure 5.5 shows simulated traces for energy depositions at different radii. The rise time of a trace is defined as the time a steep signal needs to rise from 10 to 90 % of its maximum value. Due to the different mobility of electrons and holes in the germanium, rise times vary with different radii. Since the collection time for holes is higher than for electrons and holes are collected at the outer electrode of an AGATA detector, rise times in principle decrease for increasing radii. Near the outer electrode the rise time in turn slightly increases. The kinks in the traces also originate in the different mobilities of the charge carriers. When one charge type is collected completely, the trace only depends on the remaining charge type which has a different collection behaviour. Unfortunately, these kinks are not visible in the data sets of this experiment. As it can be seen in figure 5.1, the time resolution of 25 ns per tic is too low to recognize the kinks. Therefore, the radial coordinate cannot be determined unambiguously for large radii and it is only possible to set an lower resolution limit at 190 ns in the outer part. This corresponds to a radius of about 18 mm in ring 6. Above this time limit, the rise times are well-defined and could be used for space resolved tracking.
Figure 5.6 shows the rise time spectra for all rings and for vertical hits, homonymous segments are summed up. Following geometrical estimations like for figure 4.11, the spectra show the expected trend. The vertical dashed line marks the resolution limit at 190 ns.

5.3 Reconstruction of Complete Trajectories

Completely analogous to the lateral tracking, trajectories can be visualized by plotting the rise times of the hit segments in one diagram. Figure 5.7 shows the laterally and radially tracked trajectory of a single vertical event in sector A (cf. figure 5.4(a)). Since lower rise times imply larger radii, the radial tracking shows a trajectory which starts in the inner part of segment A6 and ends in the outer layer of segment A1. The small deviation from the decreasing trend in segment A1 (between 0 and 10 mm) can be explained by the smaller dimensions of this edge segment. By combining both tracking methods, a three-dimensional trajectory can be reconstructed: starting in the left inner part of segment A6, the muon crossed the lateral and radial middle of the sector and left the detector in the far right outer part of segment A1.

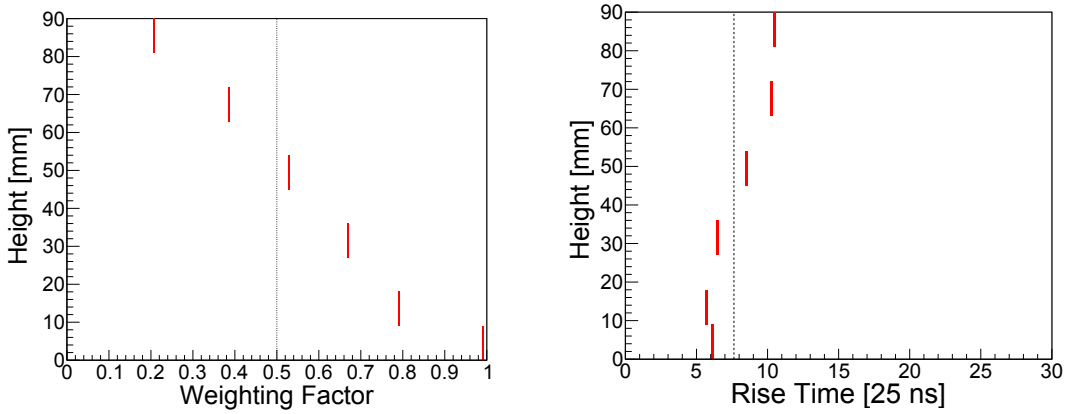

(a) (b)

Figure 5.7: The laterally tracked trajectory from 5.4(a) is extended by the associated radially tracked trajectory. Since lower rise times imply larger radii, the tracked trajectory runs from the inner left of segment A6 to the outer right of segment A1.

To conclude, the tracking algorithm is fully functional. Each segment can be divided into four subsegments for tracking purposes. Thus, the detector effectively has 144 subsegments. Additionally a radially resolved tracking is possible in the 72 inner subsegments. Yet the position calibration for the rise times has to be implemented in the algorithm. As a last step, a three-dimensional model has to be generated to fully visualise the reconstructed trajectories.

6 Summary and Outlook

The analysis performed in this work covers performance tests of the new dual gain preamplifier. The first part focuses on the general amplification properties and the determination of energy losses caused by cosmic radiation. In the second part the tracking performance inside the HPGe detector was tested and quantified.
As a first step, the condition whether a segment is considered as hit or not from [20] was optimised. Subsequently, the data set resulting from this corrected hit condition was tested in a physical context. The correction showed a clear improvement towards events which cannot be explained by linear trajectories of cosmic radiation. By gating on events with a known event path length the incoming cosmic rays could doubtlessly identified as muons. With this knowledge, the individual segments' heights could reversely be determined. Segments in ring 6 systematically deviated from the specifications. The investigation of this deviation was identified as a non-active dead layer at the intrinsic surface of the crystal, as already mentioned by Eberth and Simpson [9].
The tracking of the muons' trajectories was split in two components: the lateral tracking as a projection on the detector surface and the radial tracking. Lateral tracking was performed by comparing the transient signals in segments horizontally adjacent to a passing muon. Thus, the individual segments could be divided into two subsegments, leading to a total of 12 subsegments per existing ring in the detector. The radial tracking made use of a hit segment's signal rise time. Simulations [5] showed different rise times for different radii within the hit segments. With the simulations' results it was possible to divide the subsegments again into two subsegments with the borderline running parallel to the two electrodes. Inside the resulting inner ring of subsegments a radially position-sensitive tracking can be performed in future analysis steps. Nonetheless, the 36 segments of the detector can be divided into 144 subsegments for tracking purposes.
As a next step, it is expedient to generate a three-dimensional model of the crystal. In this model it would be easy to visualise even trajectories from non-vertical hits. For non-vertical hits lateral tracking is a bit different and the method will be discussed shortly. In a non-vertical hit the multiplicity in every ring has to be

considered additionally. If a ring's multiplicity is equal to 1, the tracking algorithm is executed as for vertical hits. For a ring multiplicity of 2 the method of comparing opposing transients is not operable. Instead the algorithm considers logically the contacting segment halfs to be crossed by the muon. Physically this has to be true for linear trajectories. Since the lateral tracking for single segment hits in a particular ring also only considers segment halfs to be directly hit, this method is reasonable. The radial tracking is still functional. The algorithm additionally refuses events with ring multiplicities of more than 2 if the segments are not directly adjacent to each other. In the horizontal consideration segments have to be at least diagonally adjacent for the event to be tracked.
The tracking analysis can be extended by a GEANT4 simulation [2] of the detector system. This collection of C++ programs includes a library for cosmic radiation and the base of the AGATA detectors is freely available for scientific simulations. In such a simulation even the detector system's surroudings (e.g. the lab's ceiling and the dewar) can be included.
With AGATA running at radioactive ion beam facilities in the future, the new dual gain preamplifier will greatly reduce background of secondary beam particles while enhancing energy resolution in higher energy regimes at the same time. Thus, the long-term goal is to introduce the tracking algorithm into the existing NARVAL framework [13] for AGATA.

Bibliography

[1] *User's Manual Digital Gamma Finder (DGF) Pixie-4*. XIA LLC, 31057 Genstar Road, Hayward, CA 94544 USA, August 2009.

[2] J. Allison and et al. Geant4, a simulation toolkit. *Nuclear Instruments and Methods in Physics Research Section A*, 506(3):250 – 303, 2003.

[3] H. Andersen and J. Ziegler. Hydrogen Stopping Powers and Ranges in All Elements. *The Stopping and Ranges of Ions in Matter*.

[4] H. Bethe and J. Ashkin. Passage of radiation through matter. *Experimental Nuclear Physics*, page 253, 1953.

[5] B. Birkenbach. Gamma ray tracking with the AGATA demonstrator - A novel approach for in-beam spectroscopy. Phd thesis, Universität zu Köln, 2014.

[6] R. Brun and F. Rademakers. ROOT - A Data Analysis Framework, 2010.

[7] A. K. De, P. Ghosh, and A. K. Das. *Journal of Physics A*, 7, 1974.

[8] G. Duchene, E. Farnea, A. Gadea, A. Korichi, J. Nyberg, P. Reiter, and J. Simpson. AGATA - Advanced GAmma Tracking Array. *Nuclear Instruments and Methods in Physics Research Section A*, 668(0):26 – 58, 2012.

[9] J. Eberth and J. Simpson. From Ge(Li) detectors to gamma-ray tracking arrays - 50 years of gamma spectroscopy with germanium detectors. *Progress in Particle and Nuclear Physics*, 60:283–337, 2008.

[10] W.-M. Yao et al. Review of Particle Physics. *Journal of Physics G*, 33, 2006.

[11] C. Amsler et al. (Particle Data Group). Review of Particle Physics, 2008-2009. *Physics Letters*, B667, 2008.

[12] J. A. Formaggio and G. P. Zeller. From eV to EeV: Neutrino cross sections across energy scales. *Reviews of Modern Physics*, 84:1307, 2012.

[13] X. Grave, R. Canedo, J.-F. Clavelin, S. Du, and E. Legay. NARVAL a modular distributed data acquisition system with Ada 95 and RTAI. In *Real Time Conference, 2005. 14th IEEE-NPSS*, page 5 pp., June 2005.

[14] D. Groom, N. Mokhov, and S. Striganov. Muon stopping power and range tables 10 MeV-100 TeV. *Atomic Data and Nuclear Data Tables*, 78:183–356, 2001.

[15] L. D. Landau. On the energy loss of fast particles by ionization. *Journal of Physics (USSR)*, 8:201, 1944.

[16] J. Lindhard, M. Scharff, and H. Schiott. Range concepts and heavy ion ranges (Notes on atomic collisions, II). *Kongelige Danske Videnskabernes Selskab: Mat.-Fys. Medd. 33*, 14:1–49, 1963.

[17] C. R. Nave. Cosmic Rays. http://hyperphysics.phy-astr.gsu.edu/hbase/astro/cosmic.html, (23.06.14).

[18] G. Pascovici, A. Pullia, F. Zocca, B. Bruyneel, and D. Bazzacco. Low noise, dual gain preamplifier with built in spectroscopic pulser for highly segmented high-purity germanium detectors. *WSEAS Transactions on Circuits and Systems*, 6 Issue 7:470–481, 2008.

[19] A. Pullia, C. Boiano, R. Bassini, and G. Pascovici. Active Reset of Digitized Preamplifiers for Ionizing-Radiation Sensors. *IEEE Transactions on Nuclear Science*, 51:831–835, 2004.

[20] D. Schneiders. Analyse von kosmischer Höhenstrahlung mit Hilfe eines segmentierten HPGe-Detektors. Bachelor thesis, Universität zu Köln, 2011.

[21] A. Wiens, H. Hess, B. Birkenbach, B. Bruyneel, J. Eberth, D. Lersch, G. Pascovici, P. Reiter, and H.-G. Thomas. The AGATA triple cluster detector. *Nuclear Instruments and Methods in Physics Research A*, 618:223–233, 2010.

[22] D. H. Wilkinson. Ionization energy loss by charged particles, Part I: The Landau distribution. *Nuclear Instruments and Methods in Physics Research A*, 383:513, 1996.

[23] F. Zocca. New technologies for low-noise wide-dynamic-range preamplification of HPGe segmented detector signals. Phd thesis, Universita degli studi di Milano, 2007.

List of Figures

Danksagung

Zuallererst bedanke ich mich bei Herrn Prof. Dr. Peter Reiter für die Betreuung und die Möglichkeit, die Thematik meiner Bachelorarbeit wieder aufgreifen und quantitativ vertiefen zu können.

Danke gebührt auch Prof. Dr. Andreas Schadschneider für die Zweitkorrektur dieser Masterarbeit.

Ich danke besonders Benedikt Birkenbach für seine umfangreiche Betreuung und zahllose Tipps und Ideen zur Programmierung und Auswertung der Daten.

Ich danke weiterhin Andreas Vogt für die fachkundige Hilfe bei der root-Integration der Messdaten und zahlreiche hilfreiche Anmerkungen zum Layout der Arbeit.

Ebenfalls bedanke ich mich bei Dr. Jürgen Eberth für die Hilfestellung bei der Bestimmung der Totschicht und die Anleitungen zum wissenschaftlichen Arbeiten.

Weiterer Dank gebührt meinen Büronachbarn Rouven Hirsch, Lars Lewandowski und Tim Steinbach für die tägliche Kollegialität und die anregenden fachlichen sowie nichtfachlichen Gespräche.

Zuletzt bedanke ich mich bei allen anderen Mitgliedern der Arbeitsgruppe, insbesondere Herbert Hess und Michael Seidlitz, für ihre Unterstützung und ihr offenes Ohr.

Erklärung

Hiermit versichere ich, die vorliegende Masterarbeit selbständig und ohne Hilfe Dritter und nur mit den angegebenen Quellen und Hilfsmitteln angefertigt zu haben. Alle Quellen und Zitate sind als solche im Text kenntlich gemacht.

Köln, im August 2014